Improved Estimates of Changes in Upper Ocean Salinity and the Hydrological Cycle

LIJING CHENG,[a,b,c] KEVIN E. TRENBERTH,[d] NICOLAS GRUBER,[e] JOHN P. ABRAHAM,[f] JOHN T. FASULLO,[d] GUANCHENG LI,[a,c] MICHAEL E. MANN,[g] XUANMING ZHAO,[a,c] AND JIANG ZHU[a,b,c]

[a] *International Center for Climate and Environment Sciences, Institute of Atmospheric Physics, Chinese Academy of Sciences, Beijing, China;* [b] *Center for Ocean Mega-Science, Chinese Academy of Sciences, Qingdao, China;* [c] *University of Chinese Academy of Sciences, Beijing, China;* [d] *National Center for Atmospheric Research, Boulder, Colorado;* [e] *Environmental Physics Group, Institute of Biogeochemistry and Pollutant Dynamics, ETH Zurich, Zürich, Switzerland;* [f] *University of St. Thomas, School of Engineering, St. Paul, Minnesota;* [g] *Department of Meteorology and Atmospheric Science, The Pennsylvania State University, University Park, Pennsylvania*

(Manuscript received 18 May 2020, in final form 17 August 2020)

ABSTRACT: Ocean salinity records the hydrological cycle and its changes, but data scarcity and the large changes in sampling make the reconstructions of long-term salinity changes challenging. Here, we present a new observational estimate of changes in ocean salinity since 1960 from the surface to 2000 m. We overcome some of the inconsistencies present in existing salinity reconstructions by using an interpolation technique that uses information on the spatiotemporal covariability of salinity taken from model simulations. The interpolation technique is comprehensively evaluated using recent Argo-dominated observations through subsample tests. The new product strengthens previous findings that ocean surface and subsurface salinity contrasts have increased (i.e., the existing salinity pattern has amplified). We quantify this contrast by assessing the difference between the salinity in regions of high and low salinity averaged over the top 2000 m, a metric we refer to as SC2000. The increase in SC2000 is highly distinguishable from the sampling error and less affected by interannual variability and sampling error than if this metric was computed just for the surface. SC2000 increased by 1.9% ± 0.6% from 1960 to 1990 and by 3.3% ± 0.4% from 1991 to 2017 (5.2% ± 0.4% for 1960–2017), indicating an acceleration of the pattern amplification in recent decades. Combining this estimate with model simulations, we show that the change in SC2000 since 1960 emerges clearly as an anthropogenic signal from the natural variability. Based on the salinity-contrast metrics and model simulations, we find a water cycle amplification of 2.6% ± 4.4% K^{-1} since 1960, with the larger error than salinity metric mainly being due to model uncertainty.

KEYWORDS: Climate change; Salinity; Climate records; Sampling

1. Introduction

The global hydrological cycle comprises the movement of water through the ocean, atmosphere, cryosphere, and land systems. It is a central element of Earth's climate system (Allen and Ingram 2002; Held and Soden 2006; Trenberth et al. 2007; Trenberth and Fasullo 2013; Marvel et al. 2017; Watanabe et al. 2018; Allan et al. 2020), yet it is also one of the most poorly observed and modeled aspects of Earth's climate system (Palmer and Stevens 2019). Models and theory predict an enhancement of the global hydrological cycle in response to global warming, including the increase of precipitation (P) intensity (Trenberth 2011) and a pattern amplification of evaporation (E) minus P (Allan et al. 2014; Held and Soden 2006).

In a warming climate, the Clausius–Clapeyron (CC) relationship predicts an increase in the water holding capacity of air (the saturation water vapor pressure) of approximately 7% per 1 K of warming (Trenberth et al. 2003). However, global total P changes are governed by an energetic constraint on evaporation, which models suggest is about 2% K^{-1} (Held and Soden 2006; Sun et al. 2012; Allan et al. 2014; DeAngelis et al. 2015; Watanabe et al. 2018). Different still, the intensity of precipitation depends upon the amount of moisture available, which is governed by the CC relationship, and feedbacks between convergence and diabatic heating (Allen and Ingram 2002; Trenberth et al. 2003, 2007; Held and Soden 2006; Allan et al. 2014). Because of the very strong patterns of precipitation (Trenberth 2011), changes in intensity are manifested mainly where it already precipitates, giving rise to the wet-get-wetter and dry-get-drier syndrome for patterns of precipitation, and thus $P - E$ changes, at least over the ocean (Trenberth 2011). A complicating factor is the effect of aerosols and their changes over time (Andrews et al. 2010; Allan et al. 2014; Watanabe et al. 2018). Some aerosols act to short-circuit the water cycle, which otherwise acts to transfer energy to the lower atmosphere via latent heating. Hence the actual outcome depends on both the amount and partitioning of aerosol species [i.e., the representative concentration pathway (RCP)] and is highly uncertain (Allan et al. 2020).

However, substantial uncertainties also exist regarding water cycle changes (DeAngelis et al. 2015; Hegerl et al. 2015) because of measurement difficulties and large spatial and

Denotes content that is immediately available upon publication as open access.

Supplemental information related to this paper is available at the Journals Online website: https://doi.org/10.1175/JCLI-D-20-0366.s1.

Corresponding author: Lijing Cheng, chenglij@mail.iap.ac.cn

DOI: 10.1175/JCLI-D-20-0366.1

temporal variability (Hegerl et al. 2015). Attributing variability is also problematic because of the uncertain impact of aerosols on clouds and radiation. Precipitation trends are reasonably well established from Global Precipitation Climatology Project (GPCP) data (Adler et al. 2018; Vose et al. 2019) and suggest that global mean trends have been small and are instead dominated by short-term variability and particularly El Niño–Southern Oscillation (ENSO).

The ocean accounts for ~80% of the global surface freshwater flux (Durack 2015). This flux has a distinct pattern with large-scale regions, such as in the subtropics, having a net negative freshwater flux ($E > P$), and large-scale regions in the higher latitudes, having a net positive freshwater flux ($E < P$). This pattern is well reflected in the ocean's salinity distribution, making salinity a powerful "rain gauge." This concept can be traced to Wust (1936) and Sverdrup et al. (1942, 124–127), who noted first the broad similarity between the mean pattern of $E - P$ and sea surface salinity (SSS). Since then, the focus has shifted to analyze ocean salinity as an indicator of the hydrological changes (Delcroix et al. 2007; Schmitt 2008; Hosoda et al. 2009; Helm et al. 2010; Yu 2011; Durack et al. 2012; Terray et al. 2012; Skliris et al. 2016; Zika et al. 2018). In fact, given that salinity integrates the highly variable E and P fields in space and time, ocean salinity is among the best recorders of long-term changes in $E - P$.

The limited number of longer-term observations of changes in ocean salinity have suggested a "fresh gets fresher, salty gets saltier" pattern (Boyer et al. 2005; Durack and Wijffels 2010; Helm et al. 2010; Durack et al. 2012; Skliris et al. 2016), in line with expectations based on changes in rainfall (wet get wetter, dry get drier; Held and Soden 2006; Trenberth 2011; Marvel et al. 2017). However, the quantification of these salinity changes, and especially of the inferred changes in the water cycle, is fraught with substantial uncertainties (Skliris et al. 2016; Zika et al. 2018). One error source is the potential data biases. These arise, for instance, from changes in the measurement system such as occurred when the traditional titration method was replaced by electronic salinometers and conductivity–temperature–depth (CTD) salinity sensors (Gouretski and Jancke 2000). Further biases might arise because of unrecognized shifts in the response of the salinometers during cruises and evaporation/condensation and chemical changes in the bottles when seawater samples are stored for a long time before analysis (Sy and Hinrichsen 1986; Gouretski and Jancke 2000). The most important source of this uncertainty is the historically relatively sparse sampling of salinity (Fig. 1, discussed later; Hegerl et al. 2015). As a result, many previous studies limited their focus on changes in surface salinity, for which the sampling is more dense than subsurface (Durack et al. 2012; Durack 2015). However, the temporal evolution of surface salinity is significantly noisier than the corresponding depth-integrated values (Yu 2011; Cheng et al. 2018), making the determination of long-term trends from surface salinity records alone uncertain.

The vertical integral approach needs to overcome the sparseness in both space and time of ocean subsurface salinity observations in the historical record (Boyer et al. 2005; Riser et al. 2016) (Fig. 1). It also needs to deal with the massive

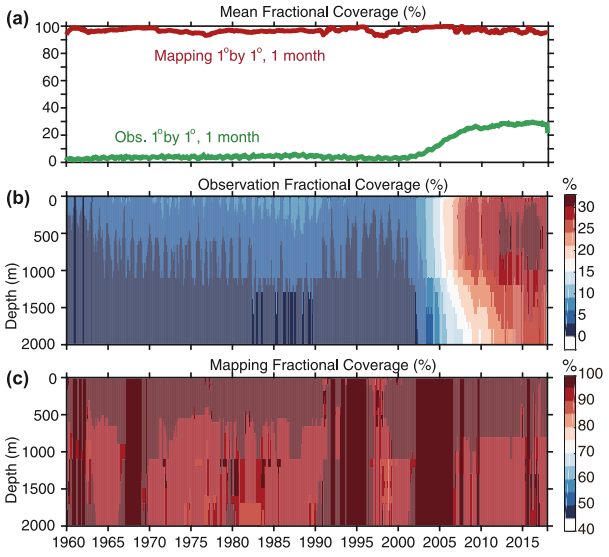

FIG. 1. Fractional coverage of the salinity observations and mapping method at upper 2000 m. (a) The 0–2000 m averaged fraction of the global ocean covered by salinity data (green) and mapping method (red) when the global ocean is divided into 1° × 1° grids within each month. (b) Monthly mean fractional coverage for salinity observations at different layers. (c) Monthly mean fractional coverage for the mapping method at different layers.

increase in sampling after the onset of Argo in 2005 (Figs. 1 and 2). Methods to overcome these sampling challenges include a widely used linear-trend infilling method (Durack and Wijffels 2010, hereafter DW10), and standard gridding procedures. However, the former method neglects the nonlinearity of climate-related trends, and the latter methods are very sensitive to the changing sampling density and method difference (Fig. 2). Moreover, the majority of the employed methods are subject to a "no data, no signal" deficiency (Durack et al. 2014; Wang et al. 2017a) whereby climate signals could be completely missed by observations. The impact of these shortcomings is not well known because many salinity reconstruction products have not been comprehensively validated. But the large spread exhibited by these products (Fig. 2; Skliris et al. 2016; Zika et al. 2018) suggests that this impact is potentially severe.

Here, we overcome these limitations by using a field reconstruction method, used in previous work to successfully reconstruct the ocean's temperature field to infer changes in the ocean's heat content (Cheng et al. 2017). We apply this method to in situ salinity observations to reconstruct monthly gridded salinity fields for the upper 2000 m since 1960. To perform interpolation across data-sparse intervals and regions, the method uses information on the spatiotemporal covariability of salinity taken from the historical coupled climate model simulations conducted as part of phase 5 of the Coupled Model Intercomparison Project (CMIP5; Taylor et al. 2012). The method is then rigorously tested using subsets of data collocated with earlier ocean observations extracted from the data-rich Argo era (as "truth"). The "sampling error" is then estimated from the difference between the reconstructed and

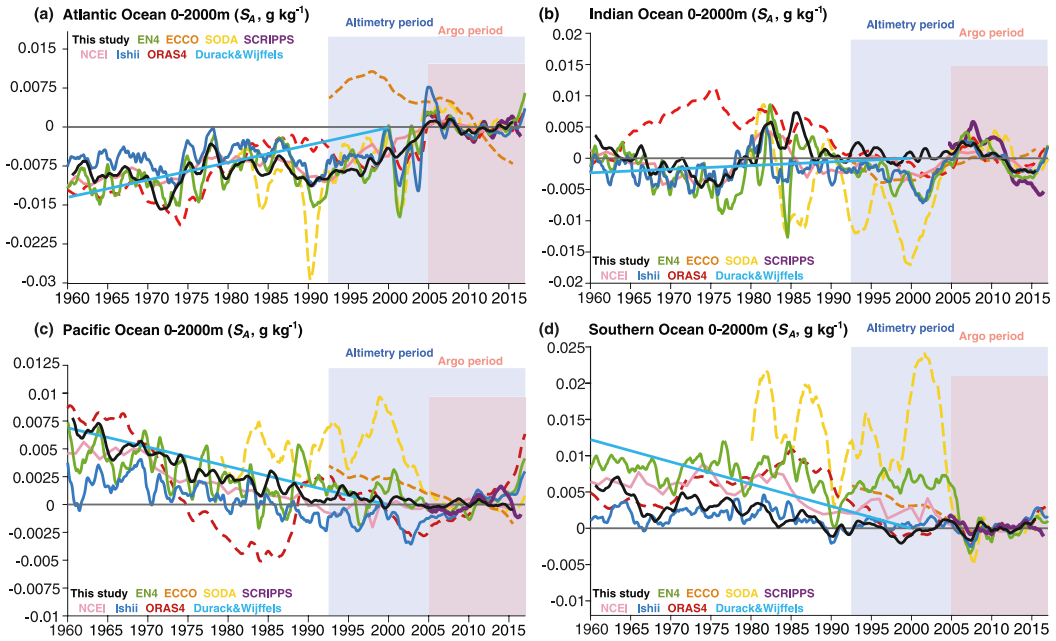

FIG. 2. The 0–2000 m mean salinity time series in the four ocean basins using different products from 1960 to 2017: (a) Atlantic Ocean, (b) Indian Ocean, (c) Pacific Ocean, and (d) Southern Ocean (70°–30°S). The products are EN4 (Good et al. 2013), Ishii (Ishii et al. 2003), ORAS4 (Balmaseda et al. 2013), ECCO (Forget et al. 2015), NCEI (Boyer et al. 2005), SCRIPPS (Roemmich and Gilson 2009), SODA (Carton et al. 2018), and DW10 linear trend (Durack and Wijffels 2010). BOA and SCRIPPS are Argo-based products, so they are only available after 2004. ECCO is from 1993 to present. All time series are 12-month running means and relative to a 2005–15 baseline.

so-called truth fields. The data and methods involved in this approach are described in section 2.

Based on our new reconstruction, we explore the global and basin-scale salinity changes averaged over the top 2000 m (S2000) in section 3a compared with estimated sampling errors to suggest a reliable reconstruction of basin integrated salinity changes since 1960. The three-dimensional changes of salinity as represented in these data are then investigated in section 3b, including spatial patterns of SSS/S2000 trends since 1960 and salinity trends for zonal–depth sections. To quantify the salinity pattern amplification, an index is adopted in section 3c to provide a new quantitative estimate of trends from 1960 to 2017 and then compared with previous study results in section 3d. In section 3e, the drivers of observed salinity changes are investigated in combination with CMIP5 simulations. In section 3f, we quantify the observed global water cycle pattern amplification. Conclusions and discussion on future work and potential improvements are provided in section 4.

2. Data and methods

a. Salinity observations

In situ ocean salinity observations are sourced from the World Ocean Database (WOD) downloaded in July 2018 (Boyer et al. 2018), with its quality flags being used to remove spurious data. Data from all available instruments (i.e., Argo, Bottle, CTD) are used in this study. Although salinities are archived in units of Practical Salinity (PSS-78, or psu), Absolute Salinity (S_A; g kg^{-1}) is adopted in this study as recommended in the Thermodynamic Equation of Seawater–2010 (TEOS-10) (McDougall et al. 2012). For the creation of gridded fields, all observations are first interpolated to 41 vertical standard levels from 1 to 2000 m.

As was done for the earlier temperature reconstruction in Cheng et al. (2017), the anomaly field is used because its spatial decorrelation scale is much larger than for climatological mean fields. Anomaly fields are obtained by subtracting a depth-dependent monthly climatology using all observations from 1990–2010 (centered at around 2000). These anomalies are averaged into a 1° × 1° grid and then input into the mapping algorithm, which infills data gaps and provides a 3D gridded field with complete spatial and temporal coverage. All data between 1990 and 2010 were used in the construction of the monthly climatology. The data were interpolated using the same new mapping method that was used for the anomalies (introduced in the next section).

The reconstruction is made separately for each month, although observations within a certain time window are combined to infill data gaps while accounting for the persistence of salinity changes over time. The size of the temporal bins (before and after) increases from 2 months at the surface to 9 months at 2000 m.

b. Mapping method

The continuity and covariability of the ocean state across spatial and temporal scales makes it possible to reconstruct the ocean state with reasonable accuracy using relatively sparse observations. A mapping method defines how the global map

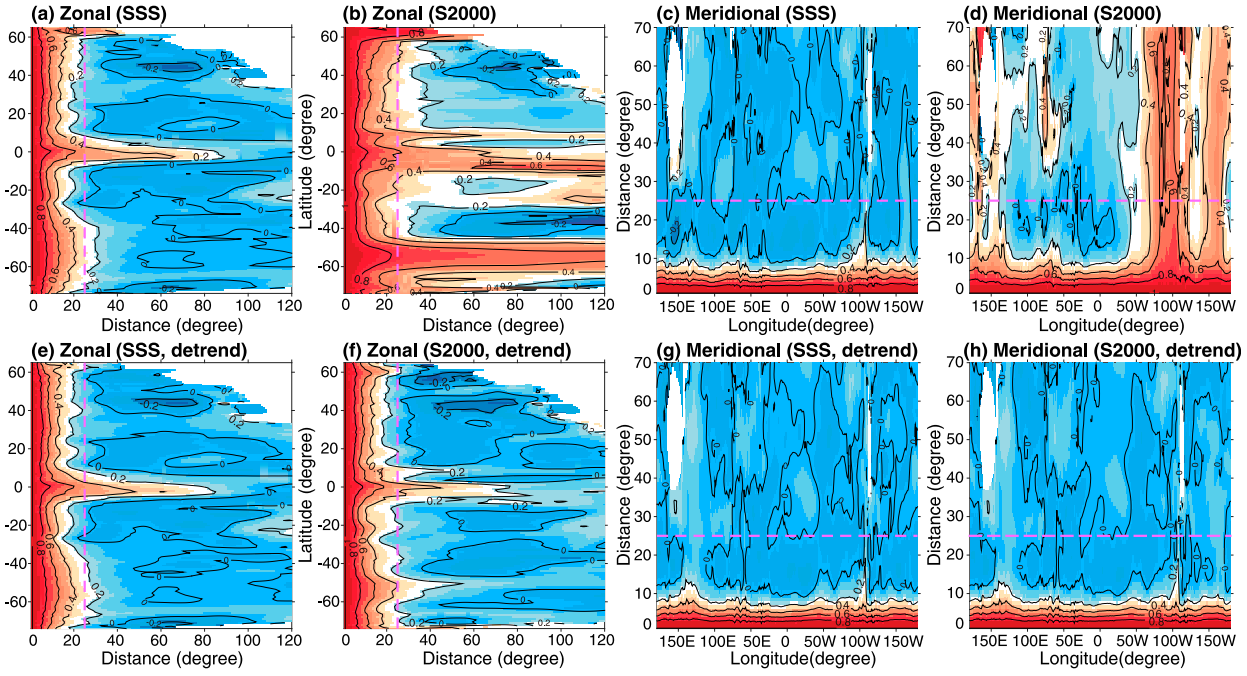

FIG. 3. (a),(b),(e),(f) Zonal-mean and (c),(d),(g),(h) meridional-mean correlation as a function of distance for (a),(e),(c),(g) SSS and (b),(f),(d),(h) S2000. The calculation is based on historical simulation for 1960–2017 (RCP4.5 for 2006–17) from the Goddard Institute for Space Studies (GISS-E2-H), but using other models shows similar results. The mean seasonal cycle has been removed when calculating the correlation. (e)–(h) Results after a linear trend is removed in each grid cell.

of a variable is created from incomplete observations and how the reconstructed field is smoothed. We follow the methodology used previously to reconstruct ocean interior temperature variations over the past few decades (Cheng et al. 2017) using an Ensemble Optimal Interpolation (EnOI) approach with a dynamic training ensemble provided by simulations of the CMIP5 models [for details, see Cheng and Zhu (2016)]. Here, we introduce the general concepts involved and outline modifications from our prior approach in its application to salinity data.

The basic framework of the EnOI method is Eq. (1): the analysis field ($\mathbf{X}^a$) is a linear combination of a prior guess field ($\mathbf{X}^b$, or background field), and the monthly gridded average in situ observations (as denoted by matrix $\mathbf{y}$):

$$\mathbf{X}^a = \mathbf{X}^b + \mathbf{K}(\mathbf{y}–\mathbf{H}\mathbf{X}^b), \tag{1}$$

where $\mathbf{H}$ is the transfer matrix from the analysis space to observation space, and the Kalman gain $\mathbf{K}$ is obtained from the maximum likelihood method by minimizing the analysis error. The Kalman gain is calculated by

$$\mathbf{K} = \mathbf{P}^b\mathbf{H}^{\mathrm{T}}(\mathbf{H}\mathbf{P}^b\mathbf{H}^{\mathrm{T}} + \mathbf{R})^{-1}. \tag{2}$$

The superscript T denotes the transpose operation; $\mathbf{R}$ is the error covariance of the observations, and $\mathbf{P}^b$ is the error covariance of the background field. The reconstructed field ($\mathbf{X}^a$) is the infilled monthly salinity anomaly and is derived from the mapping method applied to the grid-averaged salinity anomalies at each standard depth. The actual implementation follows the algorithm of Cheng and Zhu (2016) and Sakov and Oke (2008a,b), although with a somewhat modified approach, as described below. The basic formula of Eq. (1) helps to explain the concept.

The covariance ($\mathbf{P}^b$) is essential for propagating signals from data-rich areas to data-sparse regions. Previous mapping methods for ocean temperature and salinity use an empirically derived parameterized $\mathbf{P}^b$ as an approximation, which is always a distance-weighted Gaussian function, assuming isotropic spatial correlation of the ocean variability (Ishii et al. 2003; Levitus et al. 2012; Good et al. 2013). This is an oversimplified assumption, however, because the spatial covariance should be flow-dependent and much more spatially complex than a Gaussian fit. In fact, the structure cannot be explicitly characterized by idealized functions. For a brief illustration, Fig. 3 displays the zonal and meridional mean correlations of monthly salinity changes for a climate model (here the Goddard Institute for Space Studies GISS-E2-H model; other models and reanalysis data yield similar results). It is apparent that the spatial correlation scales vary widely by location.

Our modified approach therefore is to use a variety of climate models to construct a best guess for the covariance in space and time of in situ observations. With the EnOI framework, $\mathbf{X}^b$ is the ensemble mean of the CMIP5 models, and $\mathbf{P}^b$ is calculated based on the model ensemble. Here we use 43 pre-2005 CMIP5 historical (Hist) simulations along with 40 simulations from 2006 to the present under RCP4.5 projections. The models are listed in the Table S1 in the online supplemental material. Data from 1995–2005 are used to construct model

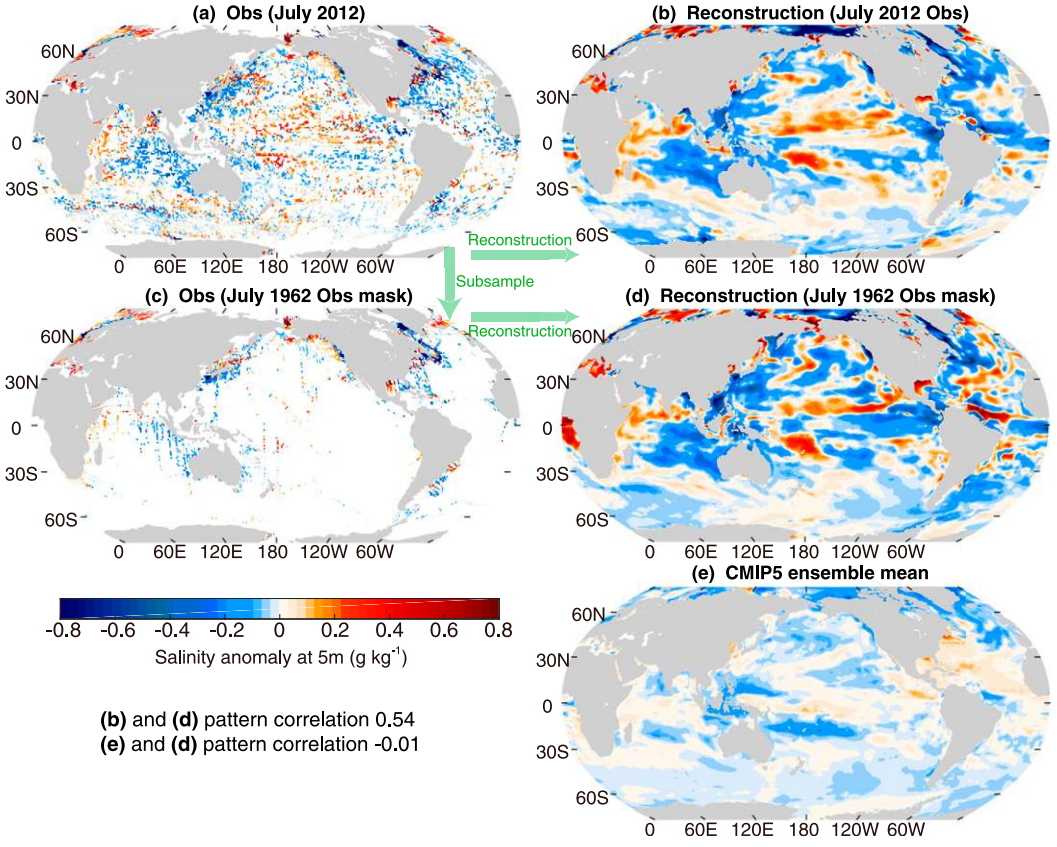

FIG. 4. Examples of the subsample test. (a) Observations and (b) reconstruction of the salinity field at 5 m in July 2012. (c) The salinity anomaly field in July 2012 was subsampled according to the location of observations in July 1962. Approximately 25% of the grids were selected during the subsample process. (d) The reconstruction based on these subsampled observations. (e) The ensemble mean of the CMIP5 models in July 2012 at 5 m depth, which is used as the prior guess in the mapping. The color shows the average salinity anomaly in each 1° × 1° grid.

climatology—centered at 2000 and consistent with observational anomalies. The window is slightly shorter than that for the observational climatology because the model historical simulations end in 2005 and there are fewer models available for RCP4.5 than Hist.

Simulations from different models sample the range of spatial covariance and the best solution is found under the constraint of observations in the EnOI framework. The models mainly provide the spatial covariance, while the model simulated temporal evolution of salinity plays a negligible role in the reconstruction. This can be confirmed by a test (Fig. 4), using the observational anomalies, the reconstruction field based on the present method, and CMIP5 model ensemble mean. By inspection, it is clear that the reconstruction field is very different from the *prior guess,* even in the regions with large data gaps such as the southeast Pacific, South Atlantic, and south Indian Oceans (Figs. 4b, d vs Fig. 4e, with a pattern correlation of −0.01). This indicates that the so-called prior guess does not impact our reconstruction in a significant manner. In the following sections, the reconstruction accuracy will be rigorously assessed by a ''subsample test.''

The key parameters for the application of this method are as follows:

1) *Localization strategy.* During the analysis of a grid cell, the mapping method uses the adjacent observations for the reconstruction by utilizing the spatial covariance, but only data within a certain spatial range are used. This strategy (termed a ''localization strategy'') is commonly adopted to avoid spurious remote correlations (Roemmich and Gilson 2009; Levitus et al. 2012; Good et al. 2013; Balmaseda et al. 2013; Forget et al. 2015; Ishii et al. 2017; Li et al. 2017). The size of the range is defined by the influence radius, which is mostly less than 8° in previous studies. Here we use a larger influence radius of 25° from the sea surface down to 2000 m, consistent with the optimal approach found in our prior temperature analysis (Cheng et al. 2017).

Using this larger influence radius allows us to leverage the large spatial covariances. Figure 3 shows the zonal mean (meridional mean) correlations at different latitudes (longitudes) as a function of distance between any two grid points. On a global average, the zonal correlations of SSS are up to ~0.3 for two

grids at a distance of 25° in the tropics (10°S–10°N) and high latitudes (70°–40°S, >60°N) (Fig. 3a). The maximum zonal mean correlation of S2000 can be as high as ~0.8 in the Southern Ocean and ~0.6 in the tropics (Fig. 3b). The correlations across latitude are much weaker than across longitude (generally less than 0.2 at 10° distance for both SSS and S2000) (Figs. 3c,d). This is a typical characteristic of ocean variability (Zang and Wunsch 2001). Compared with SSS, S2000 reveals much stronger remote covariance, for example, correlations can reach ~0.6 even at 120° in the Southern Ocean (Fig. 3b) and Atlantic Ocean (Fig. 3d). This reveals the large coherence of subsurface water mass anomalies associated with long-term trends and multidecadal variability. Removing a linear-trend from the model data results in slightly smaller zonal- and meridional-mean correlations, especially for S2000 (Figs. 3e,f vs Figs. 3a–d), but large spatial coherence persists. Further decomposing the detrended data into interannual (<8 years) and decadal time scales (>8 years) shows that decadal variability has much stronger spatial coherence than does interannual variability, but remote correlations at and beyond 25° are evident for both (Fig. S1).

Employing climate models to determine the correlation structure suggests the merit of a larger influencing radius than used in previous studies and ensures near-global fractional coverage (defined as the fraction of total ocean area obtained by the field reconstruction method) (Fig. 1). It suggests that >90% of the global ocean area at each layer for the upper 2000 m can be analyzed by this method (the unanalyzed <10% of the 1° × 1° boxes are mainly from the Arctic Ocean, which does not impact the results in this study because the area is small). This important aspect of the present analysis avoids the "conservative error," whereby the analysis field is strongly influenced by the prior guess, which occurs for most mapping methods (Durack et al. 2014; Cheng et al. 2019), an issue that will be discussed more later. Even though the larger radius results in a strong spatial smoothing, it helps to bring more adjacent observations in the analysis for a given grid cell than using a smaller radius, ensuring that the large-scale pattern is reliably reconstructed (as illustrated in Fig. 2).

2) *The observation error variance* (**R**) represents the error of the observations, including both the error due to instrument inaccuracy as well as the error caused by the need to represent the spatial structure at monthly 1° (lateral) × 1 m (depth) resolution from a limited number of observations. Here **R** is simply set to 0.01 consistently over the global ocean, assuming the error is not correlated in space. This simple assumption is made because there are insufficient data to quantify the representativeness error and the spatial correlation. As empirically identified by the International Quality Controlled Ocean Database (IQuOD) community (IQuoD 2018), the accuracy of salinity measurements ranges from 0.002 to 0.08 pss-78 depending on instruments, and therefore we adopt a value of 0.01.

We have tested the impact of this choice on the reconstruction by using two other choices (0.005 and 0.02). These additional analyses suggest a negligible sensitivity of the salinity time series derived in this study. Rather the choice of **R** mainly impacts the regional smoothness of the reconstructed fields and not the patterns, global and basin-mean or integrated quantities or their temporal variability, which are the main foci of this study. We expect to improve our estimate of **R** when more salinity observations become available (e.g., more Argo data, more data digitization, and data recovery work).

3) *Iterative strategy.* The application of a large influence radius helps to ensure a high fractional coverage but also filters out the smaller-scale signals (i.e., smaller than 25°), resulting in a smooth spatial pattern. Hence, three iterative scans are performed successively using: 25°, 8°, and 4°, to encompass ocean variability across those spatial scales. This follows the strategy adopted in our ocean temperature reconstructions (Cheng et al. 2017).
4) *The uncertainty of the reconstruction* is defined as one standard deviation (1σ) of the ensemble members after updates by the EnOI. This uncertainty mainly reflects the impact of sampling, which is the major source of error. The instrumental error is partly taken into account in the EnOI framework, as observational error covariance, and is assumed to be independent between any two grids. But potential instrumental biases in some older salinity data are not taken into account as they are seldom investigated in the current literature (Gouretski and Jancke 2000).

c. Evaluation method

Here a "subsample test" is used to understand the capabilities of the method by comparing the mapped field from a data-rich period to that reconstructed using a "resample" from that period. This resample is generated by sampling the full field of the data-rich period at the locations of the data-scarce period. This procedure is possible because after 2007, the integrated ocean observation system, including Argo and other observation networks, achieved near-global ocean data coverage for the upper 2000 m (Abraham et al. 2013; Riser et al. 2016), providing an excellent base to test the mapping method. This comprehensive and objective evaluation process is another key advantage of the data product derived in this study.

Twenty-two Argo-period salinity fields, selected every 6 months from 2007 through 2017, are used as "truth." However, because the monthly data during the Argo period do not have global coverage at 1° × 1° and monthly resolution (Fig. 1), the data within −2 to 2 months centered on each selected month are averaged to construct each so-called truth field. In this way, the fractional coverage of observations in each truth field is at least >70%.

We subsample each truth, as defined above, using different historical observation masks, selected every 30 months from 1960 to 2015 in both summer and winter. The nearest grid is used if there is no data in the truth grid. If there are more than two observations sharing the same truth, a perturbation to the subsampled data is applied using a fixed variance of 0.01 (same as value in **R**). Each subsampled field is then reconstructed by the mapping method and compared with the corresponding truth, with the difference defined as "sampling error." We use this sampling error to assess whether any trend is statistically

robust. To this end, we define a signal-to-noise ratio (SNR), computed as the standard deviation (1σ) of the salinity variability divided by 1σ of the sampling error.

This approach is sometimes referred to as a "synthetic observations" method (Cheng and Zhu 2016; Dangendorf et al. 2017; Gruber et al. 2019), where model simulation, reanalysis, or observational data with better spatial coverage are used to construct synthetic sparsely sampled observational fields. But as model or reanalysis data are limited by their resolution and systematic errors, their representativeness as the truth in the real world is limited. Here we use in situ Argo-period observations, taking advantage of their near-global ocean coverage and representativeness of the real ocean variability at all spatial and temporal scales, and estimates of instrumental errors.

An example of subsample test (Fig. 4) shows the subsampled fields and their reconstructions according to the observation locations in July 1962, compared with the corresponding truth (salinity anomalies in July 2012). The large-scale salinity anomaly pattern in July 2012 can be well reconstructed, although only ~25% of irregularly distributed observations are used (most of the data are along the coastal regions in the northwest Pacific, northwest Atlantic, and north Indian Oceans; Fig. 4c). The well-reproduced large-scale patterns in the reconstructed fields include the west–east contrasting dipole in the Indian Ocean, freshening in the western Pacific extending into the northwest/southwest Pacific, positive anomalies in the central tropical Pacific, and freshening in the tropical and midlatitude Atlantic (Fig. 4b vs Fig. 4d). The spatial correlations between the five reconstruction fields and the reconstructed truth are 0.54. Other sampling time periods (with the exception of July 1962) result in similar spatial correlations ranging from 0.40 to 0.95. There are some noteworthy uncertainties regarding the reconstructed fields in data-sparse regions. For example, in July 1962, there are few observations in the eastern Pacific Ocean, creating larger errors in the reconstruction (Fig. 4b vs Fig. 4d). Because of sparse data, some degree of reconstruction error is unavoidable. The key questions are how large the errors are and how they impact the signals of interest (i.e., large-scale patterns, global and basinwide averages). These questions are tested in a quantitative way in the following sections.

d. Independent ocean products

Several available data products are used to test our results and demonstrate the limitations of traditional mapping methods. We use six observational gridded products including EN4 from the Met Office (United Kingdom; Good et al. 2013; EN.4.2.1.g10), Ishii from Japan (Ishii et al. 2003, 2017), National Centers for Environmental Information (NCEI; United States; Boyer et al. 2005; Levitus et al. 2012), the linear trend product spanning from 1950 to 2000 for 0–2000 m from DW10, and two Argo gridded products, the Barnes objective analysis (BOA) from China (Li et al. 2017) and SCRIPPS (from the Scripps Institution of Oceanography, in the United States) (Roemmich and Gilson 2009). There are more Argo products available (https://argo.ucsd.edu/data/argo-data-products/), but as the most-used datasets offer similar depictions of temperature and salinity changes (Trenberth et al. 2016; Wang et al. 2017a,b) only two are chosen here.

Three other widely used ocean reanalysis products, which constrain numerical models with observations, are used as well: Ocean Reanalysis System 4 (ORAS4) (Balmaseda et al. 2013), Estimating the Circulation and Climate of the Ocean version 4 release 3 (ECCO v4.3) (Forget et al. 2015), and Simple Ocean Data Assimilation (SODA) (Carton et al. 2018). Throughout this study, the reanalysis products are distinguished from purely observational products.

These products cover different time periods and have different spatial and temporal resolution (Table 1). Before analysis, all data were interpolated to the IAP spatial grid and anomaly fields were used relative to their own monthly climatology based on the data from 2005 through 2017. All have been used extensively in the literature. For example, the recent Intergovernmental Panel on Climate Change (IPCC) special report for the ocean and cryosphere uses EN4 and SODA (Bindoff et al. 2019). Zika et al. (2018) use EN4 and NCEI products while Skliris et al. (2016) use EN4 and Ishii data. Vinogradova and Ponte (2017) use ECCO data. Many investigations into the mechanisms of salinity changes use ECCO, SODA, and ORAS reanalyses, which are comprehensively summarized in Yu et al. (2020). Therefore, a brief intercomparison is worthwhile.

e. CMIP5 models

We employ CMIP5 model results from the historical simulations where all forcings are considered (1960–2005; Hist) and results from the "natural" simulations where only the changes in radiative forcing caused by volcanic eruptions and changes to solar irradiance (Nat) are considered. We also use results from future projection simulations under representative concentration pathway (RCP) 2.6, 4.5, and 8.5 scenarios (Taylor et al. 2012). A list of models used is in Table S1. We employ a total of 16 models for Nat, 43 models for Hist, and 32 models for RCP2.6, 40 for RCP4.5, and 36 for RCP8.5 projections. Throughout this study, the model uncertainty is quantified by one standard deviation (1σ) of the ensemble members.

These model simulations are used in three ways. First, in the salinity mapping where data from all Hist simulations (43) within 1960–2005 and from the RCP4.5 (40) projections within 2006–17 are used in the EnOI framework. Second, to determine the emergence of an anthropogenic signal in the reconstructed salinity trends by comparing the Hist (43) and Nat (16) simulations. And third, to analyze the relationship between the changes in the ocean interior salinity contrasts with the changes in the $E - P$ contrasts. Only simulation results from those 21 models that provided data for all projections (Table S1) were used.

"Model drift" exists in climate models due to the errors in model or incomplete model spinup (Sen Gupta et al. 2013). We show results that do not apply any de-drifting process for the following reasons. 1) The metrics in this study are highly insensitive to drift because model drift is largely cancelled out by computing the differences of salinity between different oceanic regions. This is confirmed by our tests. 2) The common de-drifting process is applied for global metrics rather than regional fields, and the regional evolution of model drift is poorly known. 3) The model drift applies mainly in the deep ocean

TABLE 1. A list of observational datasets and reanalysis products used in this study and the results for salinity contrast metrics. The linear trends (g kg^{-1} century^{-1}) and percentage changes for 1960–2017 for SC2000, SC1000, SC2000-q, and SC0 are provided. The percentage change is estimated from the total change from 1960 to 2017 relative to the climatological mean from 1960 to 2017. The error bars (1σ confidence level) of linear trends are calculated by accounting for the reduction of the degrees of freedom due to the temporal correlation of the residuals. CMIP5 model results are also provided, and the model uncertainty is quantified by one standard deviation (1σ) of the ensemble members.

Dataset	Data description	Time period, spatial/temporal resolution	SC2000 (g kg^{-1} century^{-1})/percentage change (%)	SC1000 (g kg^{-1} century^{-1})/percentage change (%)	SC2000-q (g kg^{-1} century^{-1})/percentage change (%)	SC0 (g kg^{-1} century^{-1})/percentage change (%)
This study	**New observational reconstruction**	**1960–2017, 1°/monthly**	**0.028 ± 0.002/5.2% ± 0.4%**	**0.052 ± 0.006/5.4% ± 0.6%**	**0.055 ± 0.005/3.1% ± 0.3%**	**0.179 ± 0.014/7.5% ± 0.9%**
CMIP5	**Model ensemble median**	**1960–2017, 1°/monthly**	**0.021 ± 0.014/3.9% ± 2.6%**	**0.032 ± 0.024/0.9% ± 0.7%**	**0.038 ± 0.023/0.6% ± 0.3%**	**0.126 ± 0.066/5.6% ± 2.9%**
EN4 (Good et al. 2013)	Objective analyzed product based on all available ocean observations	1960–2017, 1°/monthly	0.042 ± 0.014/7.8% ± 2.6%	0.076 ± 0.024/7.7% ± 2.5%	0.077 ± 0.024/4.3% ± 1.3%	0.198 ± 0.025/7.8% ± 1.0%
Ishii (Ishii et al. 2017)	Objective analyzed product based on all available ocean observations	1960–2017, 1°/monthly	0.015 ± 0.002/2.9% ± 0.5%	0.031 ± 0.005/3.2% ± 0.5%	0.029 ± 0.005/1.7% ± 0.3%	0.092 ± 0.020/3.6% ± 0.8%
NCEI (Levitus et al. 2012)	Objective analyzed product based on all available ocean observations	1960–2016, 1°/annual	0.034 ± 0.005/6.5% ± 0.9%	0.062 ± 0.011/4.4% ± 1.7%	0.065 ± 0.010/3.3% ± 0.9%	0.247 ± 0.024/9.8% ± 1.0%
BOA (Li et al. 2017)	Objective analyzed product based on Argo data	2004–17, 1°/monthly	0.030 ± 0.009/5.9% ± 1.9%	0.042 ± 0.017/3.0% ± 1.0%	0.053 ± 0.014/1.3% ± 0.8%	0.219 ± 0.202/9.1% ± 8.4%
SCRIPPS (Roemmich and Gilson 2009)	Objective analyzed product based on Argo data	2004–17, 1°/monthly	0.036 ± 0.011/6.8% ± 2.1%	0.047 ± 0.021/6.4% ± 1.1%	0.068 ± 0.022/3.7% ± 0.6%	0.209 ± 0.283/8.7% ± 11.8%
ECCO (Forget et al. 2015)	*Ocean reanalysis, V4.3*	*1993–2015, 1°/monthly*	*0.027 ± 0.007/5.1% ± 1.2%*	*0.030 ± 0.010/3.0% ± 1.0%*	*0.023 ± 0.013/1.3% ± 0.8%*	*0.153 ± 0.065/6.2% ± 2.6%*
ORAS4 (Balmaseda et al. 2013)	*Ocean reanalysis*	*1979–2017, 1°/monthly*	*0.025 ± 0.002/4.5% ± 0.4%*	*0.043 ± 0.007/4.3% ± 0.7%*	*0.049 ± 0.004/2.7% ± 0.2%*	*0.065 ± 0.028/2.5% ± 1.1%*

below 2000 m, but our analysis focuses on the upper ocean. 4) A previous study (Durack et al. 2012) has confirmed that dedrifting does not impact the salinity analyses near the sea surface. 5) By not applying a drift correction more models can be included in the analyses, as preindustrial runs are not available for all models. 6) Current quantification of model drift correction is only an approximation, which could pose additional errors to the results. Thus, there is a trade-off between model availability of preindustrial runs and model numbers. Tests of most of the model results with and without applying a drift correction process, using a ''quadratic'' polynomial regression in each grid box subtracted from the Hist, Nat, and RCP simulations show insignificant differences. Some figures after drift correction are provided in the supplement.

f. Global mean land/ocean surface data

To quantify the global mean surface temperature (GMST) change for 1960–2017, we use (i) combined land surface air and sea surface water temperature anomalies from the National Aeronautics and Space Administration (NASA) (GISTEMP 2019), (ii) Berkley Earth (Rohde et al. 2013), (iii) Japan Meteorological Agency (JMA) data (Ishii et al. 2005), and (iv) the Cowtan–Way dataset (Cowtan and Way 2013). The linear trend is first calculated for 1960–2017 and then the total change is obtained by multiplying that rate by 58 years. The mean total warming among the four datasets is 0.88 K with a 1σ range of 0.11 K.

g. Trend calculation

An ordinary least squares (OLS) linear fit is used to calculate the linear trends. The error bars (1σ confidence level) are calculated taking account of the reduction of the degrees of freedom due to the temporal correlation of the residuals. Following Foster and Rahmstorf (2011), the noise was treated as an autoregressive moving average model: ARMA(1,1) when both lag-1 and lag-2 autocorrelations are positive; or a first-order autoregressive model, AR(1) is used when lag-1 autocorrelation is positive and lag-2 autocorrelation is negative. Simple standard error derived from OLS is used when lag-1 autocorrelation is negative (white noise).

3. Results

a. Ocean subsurface salinity changes in major basins

The reconstructed salinity averaged over the top 2000 m (i.e., S2000; Fig. 5a) decreased between 1960 and 2017 at a linear rate of $3.8 \pm 2.6 \times 10^{-3}$ g kg^{-1} century^{-1} (1σ error range). It is tempting to associate this global mean freshening to that expected from the melting of land ice. Globally, Earth's gravity satellite [Gravity Recovery and Climate Experiment (GRACE)] observed a total ocean mass increase of 2.5 ± 0.4 mm yr^{-1} since 2005, implying a reduction in ocean salinity of about $4.0 \pm 0.7 \times 10^{-3}$ g kg^{-1} century^{-1} for the upper 2000 m assuming the freshwaters are all input there (Tapley et al. 2019). But the large decadal salinity variations together with the sampling error (within -3 to 1×10^{-3} g kg^{-1} since 1960, SNR < 2) suggest that a global freshening due to land ice loss cannot yet be definitively identified, and global S2000 change could also be related to freshwater exchange between land and ocean, upper ocean, and deep ocean, or to instrumental errors.

Pronounced decadal/multidecadal trends emerge in S2000 for individual ocean basins (Figs. 5b–f and 6). S2000 decreased steadily in the Pacific basin after 1960, but sharply increased in the Atlantic basin (mostly since the 1990s) (Figs. 5b,d). These decadal variations are robust and significantly larger than the sampling uncertainty despite the evolution of the observation system (SNR $\gg 2$) (Fig. 5g) (Bryden et al. 1996; Curry et al. 2003). The increased salinity contrast between the two basins (Figs. 5b,d) has been noted before and attributed to an increased interbasin transport of water vapor from the Atlantic to the Pacific Ocean (Curry et al. 2003; Reagan et al. 2018). S2000 in the Atlantic Ocean shows larger decadal fluctuations than in the Pacific Ocean, especially in the North Atlantic, in phase with Atlantic multidecadal oscillation (AMO) (Reverdin et al. 2019; Skliris et al. 2020).

In the Indian Ocean, S2000 increased in the north (Fig. 5c), where the climatological salinity is high (Fig. 6b) and decreased in the south (Fig. 5e) where the climatological salinity is low (Fig. 6b). These opposing trends arise mainly from changes before ~1985, and are relatively robust, even though changes in the north Indian Ocean are more reliable (SNR > 2 since 1960) than in the south (SNR ~ 1 before 2005), owing to better sampling. The net salinity increase in the north, particularly in the Arabian Sea, is probably due to a trend toward stronger saline overflow from the Red Sea and Persian Gulf (DW10). In contrast, the freshening trend in the southern Indian Ocean is most likely a result of the advection of low salinity water from regions of large precipitation in the west Pacific Ocean and east Indian Ocean due to a warm ocean surface and frequent atmospheric deep convection (Cravatte et al. 2009; Du et al. 2015).

In all major basins, the SNR for interannual scale variability is less than 3 after 1960 and less robust compared with decadal/multidecadal changes. However, the North Indian and Atlantic Oceans show larger SNR than other basins, ranging from 1 to 3 after 1960 (>2 after 2005).

As the rest of this study focuses more on the spatial patterns of salinity changes, the basin-mean time series for different layers are in the supplement. In Figs. S2–S5, the basin-mean salinity changes for 0–500, 500–1000, 1000–1500, and 1500–2000 m separately compared to the estimated sampling uncertainty confirm that sampling uncertainty does not significantly impact our reconstruction for most of the ocean layers above 2000 m depth.

b. Spatial patterns of long-term salinity changes

The map of the S2000 trends over the 58 years between 1960 and 2017 (Fig. 6d) reveals even more spatial complexity of the trends, most of which seem robust as they exceed the estimated sampling error (Figs. 7 and 8). Key features include a freshening trend in the high-latitude North Atlantic that contrasts with positive trends elsewhere in the basin. The freshening trend in the Pacific is larger in the tropics and mid latitudes, whereas in the subtropical latitudes and especially the centers of the subtropical gyres, weak salinification exists (Figs. 6d,e). The map of the S2000 trend is spatially correlated (spatial

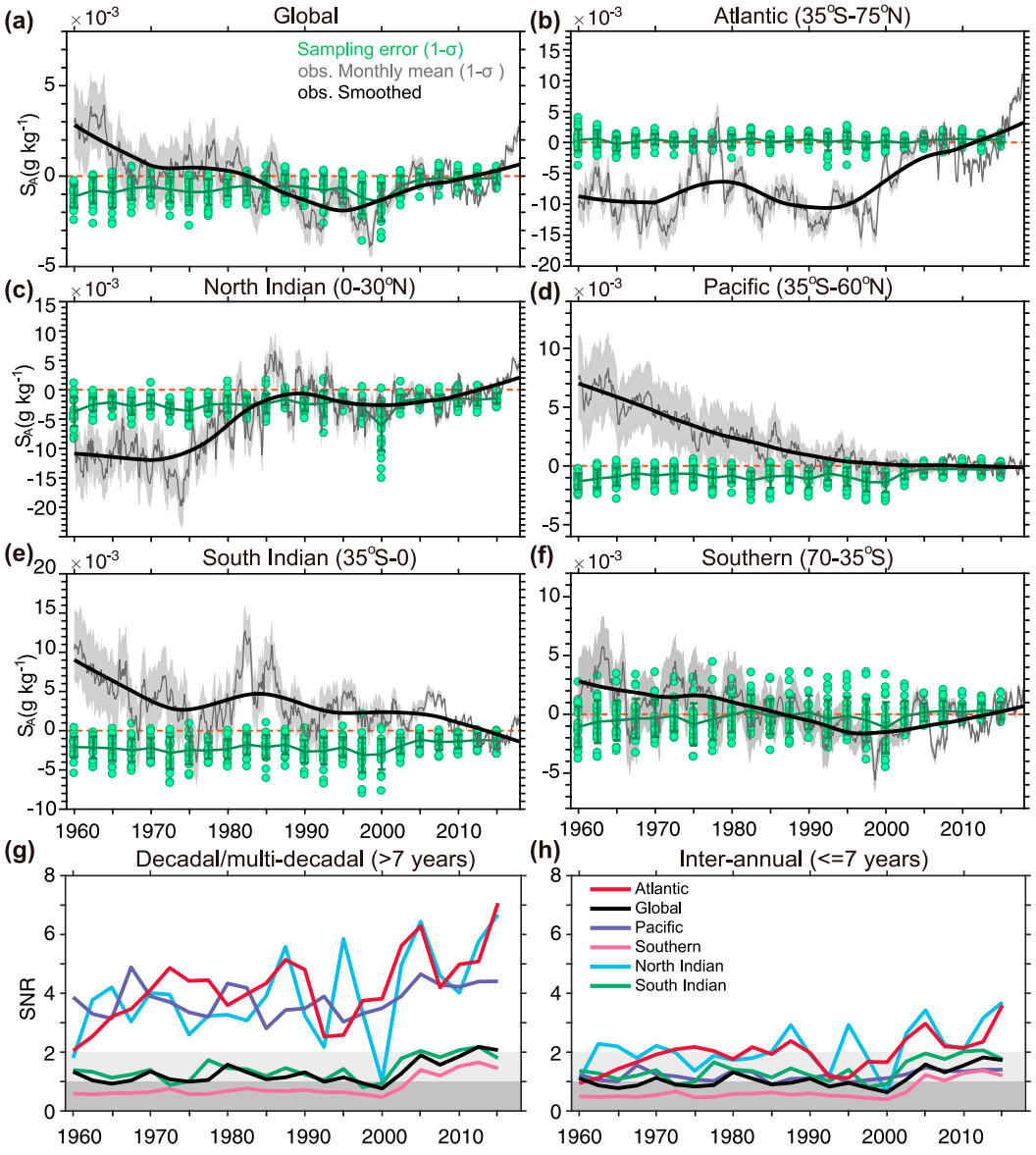

FIG. 5. Evolution of global and basin-scale 0–2000 m mean salinity and estimated sampling uncertainty. The 0–2000 m averaged salinity anomaly relative to 2008–17 for monthly time series (gray shading shows 1σ confidence interval, calculated by one standard deviation of the ensemble members) and for smoothed time series after applying a locally weighted scatterplot smoothing (LOWESS) with a span width of 240 months. (a) global, (b) Atlantic, (c) North Indian, (d) Pacific, (e) south Indian, and (f) Southern Oceans. The sampling errors use different truths (green dots), with mean and 1σ range. (g),(h) The signal-to-noise ratio (SNR) for salinity change for decadal/multidecadal (>7 yr) and interannual scales (<7 yr), respectively. SNR < 1 and < 2 are shaded.

correlation: +0.58) with the map of the SSS trends, highlighting the deep-reaching nature of the ocean salinity trends (Fig. 6c vs Fig. 6d). The two maps also have some remarkable differences, most notably a much broader band of salinification of the subtropical gyres at the surface, not seen in the depth-integrated trends. These differences likely result from the formation of anomalies near the surface and their advection and mixing into the ocean interior (Fig. 6e) (Durack and Wijffels 2010; Yu 2011; Terray et al. 2012).

Trends toward lower surface salinities in the tropics in the Pacific and Indian Oceans, where P exceeds E, form a tropical freshening band near the surface (Figs. 6c,e) and a freshening "bowl" in the upper 100 m (Fig. 6e). Salinification of waters near the surface in the subtropical gyre regions (Fig. 6c) subduct and create a high salinity "dome" in the upper 300 m within 30°S–30°N in each ocean basin (Fig. 6e) (Helm et al. 2010; Durack and Wijffels 2010). The near-surface salinification is caused by both anomalous surface freshwater fluxes and

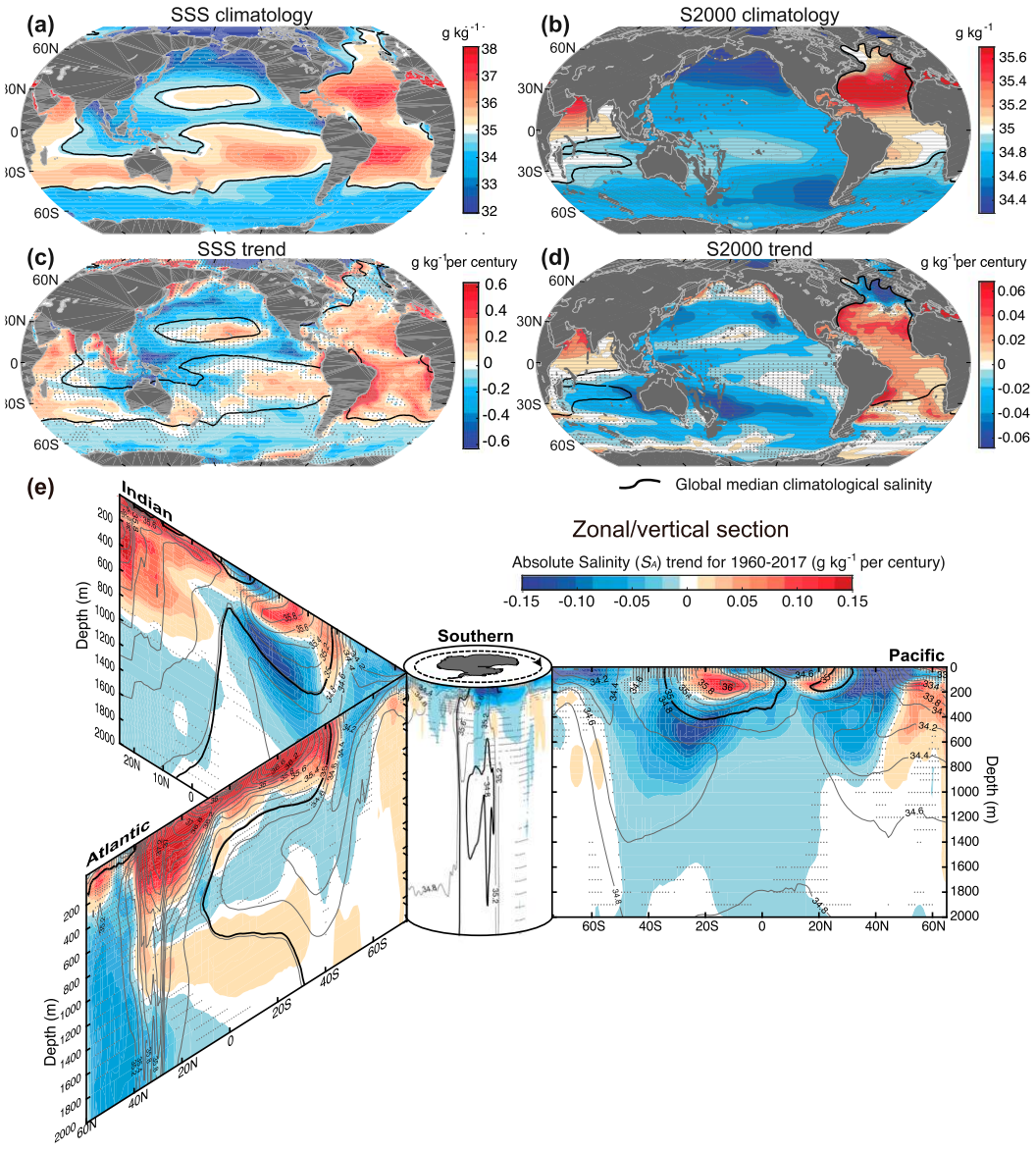

FIG. 6. Spatial pattern of the salinity climatology and long-term trend from observations. (a),(b) SSS and S2000 salinity climatology 1960–2017. (c),(d) Linear trend of SSS and S2000, for 1960 to 2017; the regions without stippling indicate the signals outside the 1σ confidence level. (e) Ocean salinity trends for 1960–2017 from sea surface to 2000 m as the zonal mean sections in each ocean basin organized around the Southern Ocean in the center. Gray contours show the climatological mean salinity, with intervals of 0.2 g kg^{-1}. The thick black contour in all panels shows the global median of the climatological salinity for SSS in (a) and (c) and S2000 in (b), (d), and (e).

warming-induced poleward isopycnal movements (Durack et al. 2010; Zika et al. 2018). Freshening of the low-salinity intermediate waters at latitudes poleward of 30° that then sink in the Southern Ocean and North Pacific/Atlantic creates a broad freshening from 500 to 2000 m in each basin (Figs. 6d,e). These changes indicate a close connection between high-latitude near-surface changes with low-latitude subsurface anomalies, where subpolar and subtropical surface anomalies could penetrate equatorward along isopycnals (Durack et al. 2010; Helm et al. 2010). One exception is a middepth salinification trend in the Atlantic, most likely caused by an enhanced intrusion of the saline Mediterranean Outflow Water (MOW), which extends from the Mediterranean Sea (where $E \gg P$) at ~35°N into the 800–1500 m layer in the Atlantic Ocean (Fig. 6e) (Durack et al. 2010; Skliris et al. 2014). In the Southern Ocean, there is a broad freshening in the upper 200 m and a salinity increase below 200 m, across basins, primarily driven by a surface flux associated with ocean advection and perhaps enhanced sea ice melt, while ice-sheet melt plays a much smaller role (Haumann et al. 2016; Swart et al. 2018). The vertically opposing changes compensate and result in a less-identifiable net S2000 change compared to sampling error (Fig. 6f).

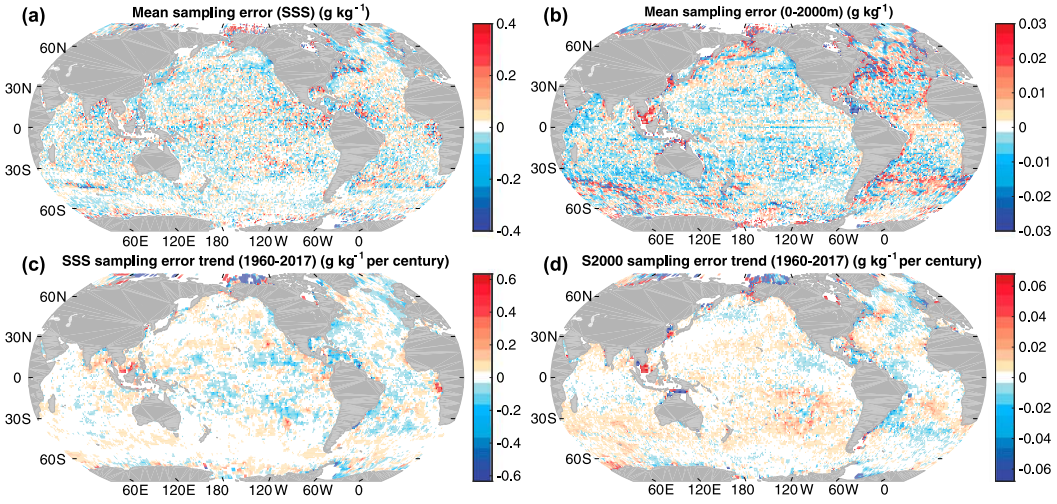

FIG. 7. Geographical distribution of sampling error. (a),(b) Mean and (c),(d) linear trend of the sampling error (left) at sea surface (to be compared with SSS) and (right) for 0–2000 m mean (to be compared with S2000) at each $1° \times 1°$ grid.

Next, we consider the geographical distributions of the surface and the 0–2000 m mean sampling errors and their trends since 1960, to evaluate the robustness of the signals detected above. For SSS, no significant bias exists over the global ocean (Fig. 7a). Note that the magnitude of the local $1° \times 1°$ mean errors is larger than the global or basin salinity means (shown in Fig. 5), because the regional errors/noise tend to cancel when taking an average over a large area. Also, the trends due to the change of sampling over time show much weaker and distinctive patterns (Fig. 7c, mostly less than $0.1\,\mathrm{g\,kg^{-1}\,century^{-1}}$) compared with the observational trends (Fig. 6c), indicating no significant local spurious trends.

For S2000, small systematic negative errors exist in the midlatitudes of the Southern Hemisphere and north Indian Ocean (Fig. 7b) and also in the basin means below 500 m (Figs. S2–S5c–f). This negative sampling bias is probably

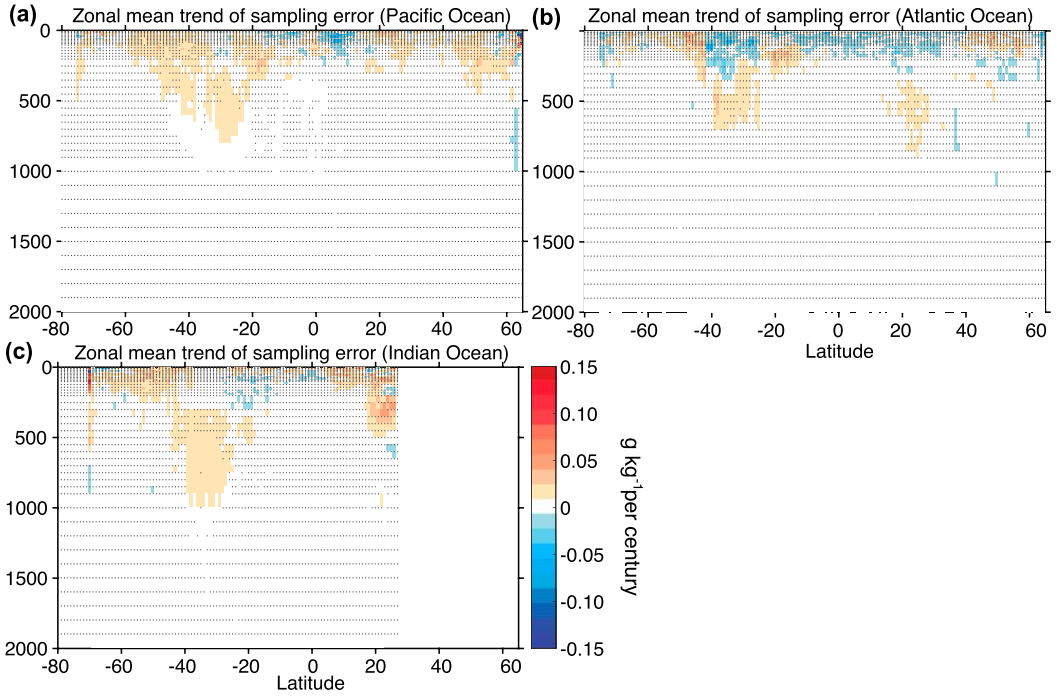

FIG. 8. Zonal mean trend of the mean sampling error for 1960–2017 from sea surface to 2000 m, for the (a) Pacific Ocean, (b) Atlantic Ocean, and (c) Indian Ocean. The nonstippled regions show the trend sourced from sampling error is outside the 1σ confidence level. The color bar is as in Fig. 2e.

related to the errors in the CMIP5 models used to obtain the spatial correlation structures. Sampling error changes over time and induces a weak positive trend in these locations (Fig. 7d). However, this time-variable bias (mostly less than 0.01 g kg^{-1} century^{-1}) is much smaller than the observed salinity trend identified in Fig. 6d. Thus, the small spurious trend identified here does not impact the results in this study. Its spatial pattern is also distinguishable from the long-term salinity trends, suggesting the robustness of the identified salinity pattern. Nevertheless, care should be taken if salinity changes are investigated for only a small region, especially in the mid- to high latitudes in the Southern Hemisphere.

For zonal–depth sections, the sampling error reveals a very small and negligible error for the long-term trend in all three basins (Fig. 8 vs Fig. 6e). There is a small spurious positive (salty) bias for the long-term trends from 300 to 1000 m within 20°–40°S in all three ocean basins (<0.04 g kg^{-1} century^{-1}; Fig. 8). However, the reconstructed long-term salinity trends (Fig. 6e) are always much larger than this error. For example, at the same location, the Pacific has a strong freshening trend of >0.10 g kg^{-1} century^{-1} above 1000 m (Fig. 6e), and the Atlantic Ocean has a strong salinification trend for the upper 600 m (>0.10 g kg^{-1} century^{-1}) (Fig. 6e). In the North Atlantic Ocean, the salinification trend gets weaker below 600 m (0.02–0.04 g kg^{-1} century^{-1}) but extends to 1200 m into the lower latitudes and Southern Hemisphere; such a structure makes physical sense and is related to Mediterranean Sea outflows (Fig. 6e) (Durack et al. 2010). The pattern is distinctive from the sampling error. An additional small distinguishable negative error occurs at 20°S–20°N in all basins in the upper 200 m (<−0.02 g kg^{-1} century^{-1}; Fig. 8 vs Fig. 6e). Therefore, this test indicates an insignificant impact of sampling error on the vertical–zonal salinity trend diagnosed by the new analysis. The climate-related patterns (Fig. 6) are confirmed to be reliable and not due to sampling errors.

In summary, with a carefully designed evaluation process, the results substantially strengthen and refine the well-established picture of long-term salinity change structures (Boyer et al. 2005; DW10; Skliris et al. 2014). The main concept is that the surface amplification patterns are subducted via normal gyre ventilation [see the Fifth Assessment Report of the IPCC (IPCC AR5) (Rhein et al. 2013) and the recent ocean and cryosphere special report (IPCC 2019)], leading to broad freshening of the intermediate waters in all basins from 300 to 2000 m within 40°S–40°N (except MOW-induced salinification within 800–1500 m in the Atlantic Ocean), and salinification in the subtropical gyres. Moreover, the new product contains mostly insignificant sampling errors, and is therefore useful for the quantification of ocean subsurface salinity changes in the upper 2000 m since 1960, especially for decadal and multidecadal scales.

c. *Quantification of salinity pattern amplification*

Overall, our new ocean salinity reconstruction confirms, with much higher confidence, the demonstrated "fresh gets fresher, salty gets saltier" pattern. That is, the trend from 1960 to 2017 has amplified the mean ocean salinity patterns. To capture this amplification change, we apply an index to our new observational analysis, named the Salinity Contrast (SC) index.

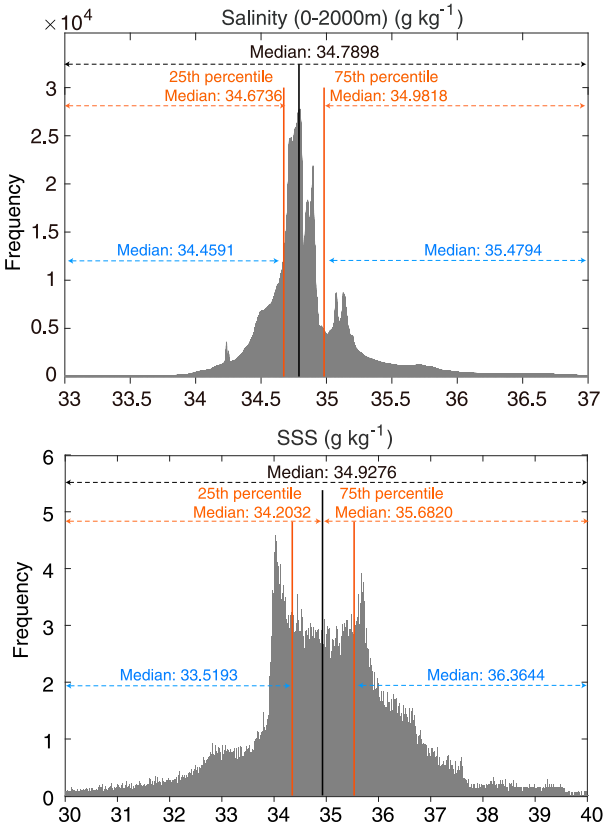

FIG. 9. Frequency distribution of salinity in (top) 0–2000 m global ocean volume and (bottom) a 2D plane at the sea surface (SSS) from observational climatology. The x axis is the salinity with an interval of 0.0002 g kg^{-1}. The frequency on the y axis is defined as the number of grid cells (weighted by the fraction of the grid area against global ocean area) with mean salinity falling into each salinity interval in the x axis. For S2000m, each 0–2000 m salinity profile in each grid box was first interpolated into 1-m-interval depths, so the statistic was done for 3D grid cells (each cell with a size of 1° × 1° horizontally and 1 m vertically). The median, 25th percentile, and 75th percentile are shown in orange. In addition, the median salinity <25th percentile and >75th percentile are also provided in blue. Those numbers were used in the calculation of salinity contrast metrics.

The SC is defined as the difference between the salinity averaged over high-salinity (V_{High}, where salinity is higher than a climatological global median, S_{clim}) and low-salinity (V_{Low}, where salinity is below S_{clim}) regions. It is calculated each month over the three-dimensional (x, y, z) ocean salinity field:

$$\mathrm{SC}(t) = \frac{\iiint_{V_{\mathrm{High}}} S(x,y,z,t)\,dV}{\iiint_{V_{\mathrm{High}}} dV} - \frac{\iiint_{V_{\mathrm{Low}}} S(x,y,z,t)\,dV}{\iiint_{V_{\mathrm{Low}}} dV}, \quad (3)$$

where x, y, and z are the three dimensions of latitude, longitude, and depth, respectively. The terms S_{clim}, V_{High}, and V_{low} are all determined on the basis of the climatological salinity field during 1960–2017 (Fig. 9). The 1960–2017 climatology is a

simple average of the reconstructed gridded fields within this period. This amplification index can be calculated for any ocean volume, either over the sea surface alone (termed as SC0) or over the volume, from the surface down to any depth (termed SC2000 for 0–2000 m volume, SC1000 for 0–1000 m volume, etc.). This index can also be calculated for different percentiles, such as SC2000-q, where V_{High} and V_{low} are defined as <25th- and >75th-quartile regions (Fig. 9). It can also be extended to potential density coordinates rather than z coordinates. We will focus mainly on SC2000 and SC0 for clarity in this study but also provide SC1000 and SC2000-q results in Table 1 and the online supplement.

A constant S_{clim} assumes that the global median salinity does not change significantly over time, an assumption supported by Fig. 5 and IPCC AR5 (Rhein et al. 2013). Most CMIP5 models show a very small global salinity decrease of $\sim 10^{-6}$ g kg^{-1} yr^{-1}, although they do not have interactive ice sheets. A test using the time-variable S_{clim} calculated for each month shows less than 5% difference in the SC2000 trend, but fixed V_{High} and V_{low} have considerable merit because it is easier to calculate SC2000. A similar index was used in IPCC AR5 but for SSS only (corresponding to SC0 in this study). A physical motivation for SC is provided by Zika et al. (2015), who found a linear relationship between increases in the mean deviation of full depth ocean salinity and water cycle amplification and that it is invariant to changes in ocean circulation. The two metrics, SC and mean deviation, are mathematically equal when the mean and median of S_{clim} are equal.

SC2000 increased substantially from 1960 to 2017, with a highly significant linear trend of 0.028 ± 0.002 g kg^{-1} century^{-1} (1σ error bar) that is not impacted by sampling error (Fig. 10a, Table 1). The SNR for SC2000 changes on decadal/multidecadal scales is ~6 before 2005 and ~10 after 2005, larger than any of the global and basin means (Fig. 10a vs Fig. 5), making SC2000 a very robust metric of ocean salinity changes. In absolute terms, the contrast between the low and high salinity regions increased over these 58 years by ~0.016 g kg^{-1}. This represents a total change of 5.26% ± 0.4% in the mean contrast (Fig. 10a, Table 1). After 1991, the rate of increase accelerated, with a trend (0.035 ± 0.004 g kg^{-1} century^{-1}) that is twice that of the 1960–90 period (0.019 ± 0.006 g kg^{-1} century^{-1}). Correspondingly, 2/3 of the total SC2000 increase since 1960 occurs after 1991 (3.3% ± 0.4% from 1991 to 2017 vs 1.9% ± 0.6% from 1960 to 1990).

The surface ocean contrast between high and low salinity regions (i.e., SC0; Fig. 10b, Table 1) also increased with a statistically significant trend (0.179 ± 0.014 g kg^{-1} century^{-1}; a total of 7.5% ± 0.9% increase of mean SSS contrast within 1960–2017), confirming findings of the IPCC AR5 for 1970–2010. The SNR for SC0 is 2–4 before 2005 and 6–8 after 2005 on decadal/multidecadal scales, about half that of SC2000, indicating less reliability of this surface metric. Again, the sampling error gets smaller after 2005 with the Argo network.

The SC0 trend is also more strongly affected by short-term fluctuations (i.e., interannual variability) (Figs. 10a,b) than SC2000, as expected from the direct exposure to fluctuations in E and P. This difference is well illustrated by the emergence of long-term trends with respect to the noise, represented by the

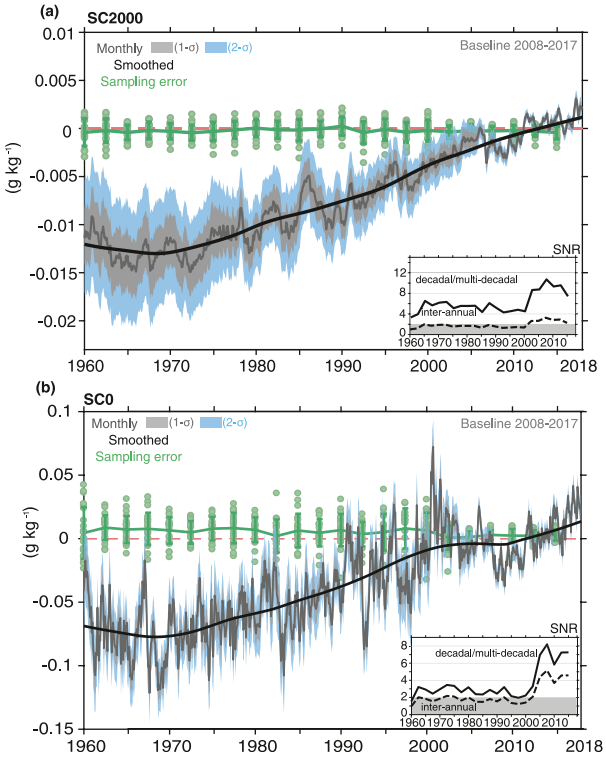

FIG. 10. Salinity-contrast time series from 1960 to 2017 (a) at the upper 2000 m and (b) at the surface. Monthly anomaly time series and its 1σ and 2σ error bars relative to a 2008–17 baseline. The inset box shows the SNR for salinity change on decadal/multidecadal (>7 years; solid line) and interannual scales (<7 years; dashed line). SNR < 2 are shaded. Green dots represent the sampling errors corresponding to 22 different "truth" fields, accompanied with mean as lines and the 1σ error bars. The dark black line is the time series after applying a LOWESS with a span width of 240 months.

standard deviation of the year-to-year fluctuations. Thus, it takes ~11 years for the SC2000 signal to emerge from the noise (when the signal is 2 times larger than noise, at 95% confidence level) but twice as long (~24 years) for the SC0 signal to emerge. Hence the integrated subsurface metric is a more robust metric of change.

The SSS pattern intensification is stronger (7.5% ± 0.9% for SC0) than subsurface changes (5.2% ± 0.4% for SC2000, 5.4% ± 0.6% for SC1000, and 3.1% ± 0.3% for SC2000-q; Table 1) for the 1960–2017 period, probably because this is a transient system response with near surface waters being in close equilibrium with the current warmer atmosphere and deep waters in equilibrium with the past cooler atmosphere (Zika et al. 2018). Therefore, the surface salinity pattern amplification is exacerbated by ocean warming and ice melt (Zika et al. 2018).

d. A comparison with other available products

There is a large spread in previous estimates of SSS and subsurface salinity pattern amplification, which challenges the reliability of previous estimates (e.g., Durack et al. 2012; Skliris et al. 2016; Vinogradova and Ponte 2017; Zika et al. 2018).

Here we first analyze salinity time series from different products to gain more insight into the data uncertainty (Fig. 2; S2000 in four major ocean basins). Some products have dramatic shifts around 2005 that are unreasonably large and impact trends, for example, in the Atlantic Ocean (Fig. 2a; EN4, Ishii, and SODA), Southern Ocean (Fig. 2d, EN4, SODA, NCEI, and ECCO), and Pacific Ocean (Fig. 2c; SODA and ORAS4). ORAS4 also reveals a large regime shift around 1993, associated with the inclusion of altimetry data. DW10 show a much stronger long-term increasing trend in the Atlantic Ocean and downward trend in the Southern Ocean than all other products, which could explain why a stronger estimate of SSS pattern amplification was obtained using DW10 data compared with other products (Durack et al. 2012; Skliris et al. 2016; Zika et al. 2018). The difference between ECCO data and other products explains why Vinogradova and Ponte (2017) found a large negative estimate on the salinity pattern amplification in the North Atlantic Ocean. The fluctuations in SODA data are much larger than other data in all ocean basins and considered untrustworthy.

For SC2000 and SC0 time series, which are more relevant to the salinity pattern changes, these products are quite consistent during the data-rich Argo period after 2005, but diverge in prior decades (Fig. 11). For SC2000, the NCEI estimate is closest to our new product, probably because it is a pentadal product. EN4/SODA shows a very large spurious upward shift during 2000–05, resulting in a much stronger SC2000 increase than other data. Among all these products, the new reconstruction shows much better continuity during the periods of observing-system change such as 1993 (altimetry) and 2005 or so (Argo), which is more physically tenable. The spread of the linear rates of SC2000 is from 0.015 to 0.042 g kg^{-1} century^{-1} (0.065 to 0.247 g kg^{-1} century^{-1} for S0), equivalent to an amplification of 2.9%–7.8% (2.5%–9.8%) (Table 1; SODA is excluded here). This large spread is consistent with previous estimates of surface and full-depth salinity pattern amplification, for example 5.0%–8.0% across Zika et al. (2018) and Durack et al. (2012) for surface salinity change since the 1950s (Table 2).

Most prior methods used relatively small influence radii (<10°), which leads to a low fractional areal coverage of much less than 90%. Consequently, the reconstructions tend to be biased toward their prior guess (“no data, no signal” deficiency) (Cheng and Zhu 2014; Durack et al. 2014; Palmer et al. 2015; Meyssignac et al. 2019). For example, the difference of the salinity field between August 1971 and August 1991 at 1500 m depth for EN4, Ishii, and the new data (Fig. 12) should be smaller in the Pacific Ocean than in the Atlantic Ocean due to the slower water mass formation in the Pacific Ocean as a physical benchmark. However, first, Ishii and EN4 data are close to zero in the southeast Pacific, where there are large data gaps in both years (Fig. 12) indicating that the reconstruction is closer to their prior guess. Good et al. (2013) explicitly state, regarding EN4, that it is “important to note that the analyses will relax to climatology in the absence of any observations” (p. 6707). Second, EN4 data show spotty salinity anomalies in the Pacific Ocean (Fig. 12) at the locations where there are data for only one year. The magnitude of the Pacific salinity anomalies

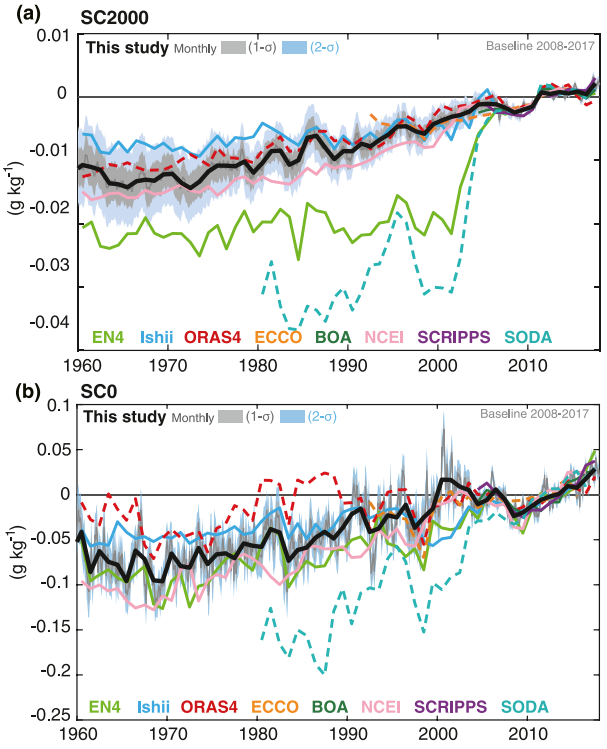

FIG. 11. Annual mean time series of (a) SC2000 and (b) SC0 for different products. The products include EN4 (Good et al. 2013), Ishii (Ishii et al. 2003), ORAS4 (Balmaseda et al. 2013), ECCO (Forget et al. 2015), BOA (Li et al. 2017), NCEI (Boyer et al. 2005), SCRIPPS (Roemmich and Gilson 2009), and SODA (Carton et al. 2018). BOA and SCRIPPS are Argo-based products, so they are only available after 2004. ECCO is from 1993 to the present. The monthly (together with the 1σ and 2σ uncertainty ranges) and annual time series from this study are also shown. All time series are relative to a 2008–17 baseline.

is as large as in the Atlantic Ocean, which is most likely unphysical and at odds with Ishii and the present data. By contrast, the data of this study show greater uniformity in the Pacific Ocean, which is more physically correct.

In summary, our investigations suggest that the errors in traditional datasets are mainly responsible for the large spread in previous quantifications of the salinity pattern amplification, and our new product is more reliable for examining long-term salinity changes.

e. Attribution of the salinity change to human influence

Are these multidecadal trends in the salinity contrast driven by natural (volcanic, solar, and internal variability in the climate system) or human (greenhouse gases, aerosols, and land use) radiative forcing changes? We use coupled climate model simulations from CMIP5 (Taylor et al. 2012) to address this question, by contrasting the historical simulations (CMIP5-Hist) that included all forcings, including the anthropogenic contributions, with the natural-forcing only simulations (CMIP5-Nat). Only the CMIP5-Hist simulations are able to capture the observed trends; that is, they reveal that the salinification and freshening trends occur in the saltier and fresher

TABLE 2. A summary of the observational estimates on salinity pattern amplification and water cycle intensification.

	Salinity data	Method to derive $E - P$ change from salinity data	Time period	Salinity pattern amplification	Water cycle intensification
This study	This study	Regression between salinity contrast and $E - P$ change in CMIP5 model ensemble mean	1960–2017	7.5% ± 0.9% (SC0) 5.2% ± 0.4% (SC2000) 3.1% ± 0.3% (SC2000-q) 5.4% ± 0.6% (SC1000)	2.6% ± 2.0% K^{-1} (SC0) 2.6% ± 4.4% K^{-1} (SC2000) 3.2% ± 3.4% K^{-1} (SC2000-q) 2.8% ± 3.0% K^{-1} (SC1000)
Durack et al. (2012) SSS zonal (SSSz) mean pattern amplification	Linear trend data from Durack et al. (2010)	Regression between zonal mean SSS change and $E - P$ change in CMIP5 models, weighted by the pattern correlation	1950–2000	8% (SSSz)	8% ± 5% K^{-1}
Skliris et al. (2014) SSS zonal mean pattern amplification	Linear trend data from Durack et al. (2010)	Similar to Durack et al. (2012)	1950–2010	5.3% (SSSz)	4.7% K^{-1}
Skliris et al. (2016) Full-depth salinity pattern amplification	Ishii, EN4 and DW10 data	Water mass transformation theory	1950–2010	—	3.0% ± 1.6% K^{-1}
Zika et al. (2018) SSS pattern amplification	EN4 gridded data	Water mass transformation theory	1957–2016	5.0% ± 1.1% (SSS)	3.6% ± 2.1% K^{-1}
Zika et al. (2018) SSS pattern amplification	Boyer et al. (2005) data	Water mass transformation theory	1955–98	5.4% (SSS)	—
Hosoda et al. (2009) SSS pattern amplification	Argo and other hydrological data	Surface salinity budget equation	2003–07 vs 1960–89	5.5% (SSS)	3.7% ± 4.6%

regions, respectively (Figs. 13 and 14 vs Fig. 6). In contrast, CMIP5-Nat show only weak trends, with a distinctly different spatial pattern (Figs. 13 and 14). Correcting model drift results in negligible impacts on the spatial patterns (see Fig. S6). Although broadly consistent with observations, CMIP5-Hist shows some regional biases (Fig. 13a vs Fig. 6e), including much weaker salinification in the subtropical gyres of the Pacific Ocean and a freshening bias in the north Indian Ocean. These biases mainly occur near the surface, implying that surface forcing ($E - P$) biases in models might be responsible. Hence the observed amplification of the salinity pattern cannot be explained in terms of only natural variability and changes in natural forcing.

Using global metrics, the CMIP5-Hist results show a robust increase in SC2000 and SC0, with the median from all individual model trends of 0.021 ± 0.014 g kg^{-1} century^{-1} (SC2000; 3.9% ± 2.6%) and 0.126 ± 0.066 g kg^{-1} century^{-1} (SC0; 5.6% ± 2.9%), where the error bar is the 1σ spread across all models (Fig. 15). The models have slightly weaker trends than the observational estimates, but are consistent, given the uncertainty range. In contrast, for CMIP5-Nat, there are no statistically significant trends (Fig. 15). CMIP5-Hist also suggests a rate increase of SC2000 by 1.5 times after 1991, consistent with observations. For both SC0 and SC2000, the median trends of both CMIP5-Hist and current results exceed the 2σ natural range (>95% confidence level) (Figs. 15c,d), which suggests that since 1960 the anthropogenic signal in ocean subsurface salinity has emerged from the natural background variability. Although several models show large adjustments with corrections for model drift, the model ensemble median is nearly identical to the results without corrections for both Hist and Nat (Fig. S7).

Six out of seven independent salinity reconstruction products show a SC2000 (five for SC0) increase in the past decades that exceeds the 2σ natural range (Figs. 15c,d, Fig. S8 for SC1000 and SC2000-q). This reinforces our results and confirms that the new subsurface indices are a particularly robust and attributable metric of the ''human fingerprint'' of the climate system, extending previous results (Barnett et al. 2001; Curry et al. 2003; Pierce et al. 2012; Stott et al. 2008).

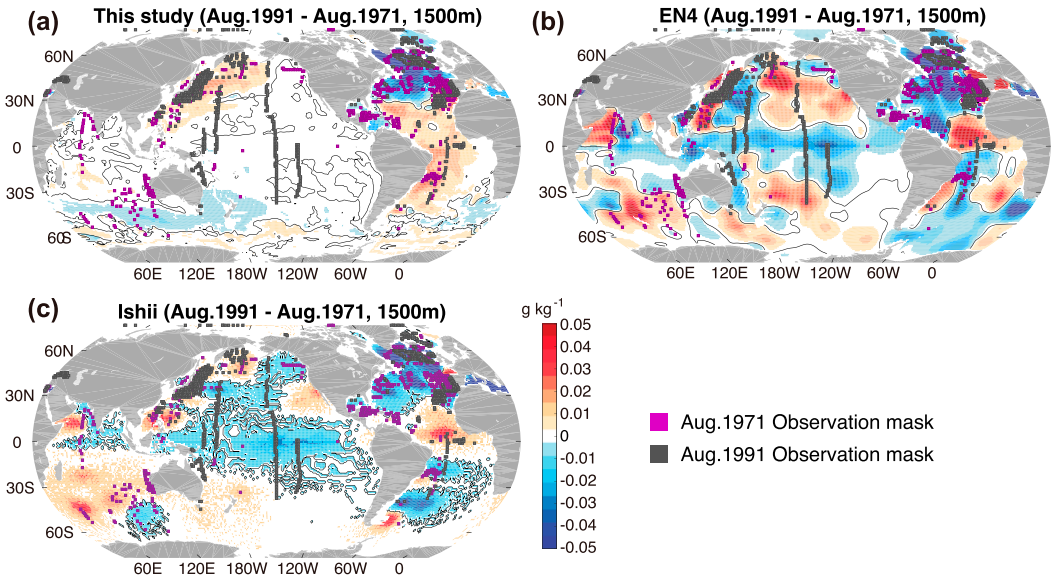

FIG. 12. Salinity difference between August 1991 and August 1971 at 1500 m depth for (a) the data in this study and the (b) EN4 and (c) Ishii data. The purple (black) dots are the observation locations in August 1971 (August 1991) from WOD. The near-zero anomalies are evident in data-sparse regions in the southeast Pacific Ocean in this example for EN4 and Ishii, which is the indicator of the conservative bias. The contour shows zero anomaly.

Moreover, the attribution metric is easily implemented and has less/negligible sampling error.

f. Salinity change as an indicator of changes in the hydrological cycle

Many different methods have been proposed to quantify the hydrological cycle amplification on the basis of ocean salinity changes (Durack et al. 2012; Skliris et al. 2016; Vinogradova and Ponte 2017; Zika et al. 2018). Here we use the SC metric along with a similar $E - P$ contrast metric, defined as the difference between $E - P$ averaged over higher versus lower $E - P$ regions relative to the ocean global median.

We use the observed salinity change and the slope of the regression between the model-based salinity contrasts and the $E - P$ contrasts to determine $E - P$ change since 1960. The salinity–$E - P$ regression is obtained by an OLS fit of model simulations for the period 1960–2030 for Hist, RCP2.6, 4.5, and 8.5 together (Fig. 16), or within 1960–2005 for Hist only. The uncertainty range of the salinity–$E - P$ relation is determined from the 1σ model spread. And the uncertainty range in derived $E - P$ change is calculated by a Monte Carlo simulation considering the uncertainty in both observational salinity contrasts trend and the model-based salinity–$E - P$ correlation. For the Monte Carlo simulation, 50 000 realizations were performed. We assumed a Gaussian distribution for both the salinity trend and the salinity–$E - P$ regression.

The models reveal a clear positive correlation between the salinity contrast metrics SC2000 and SC0 and this $E - P$ contrast (Fig. 16), with a linear regression slope of 1.49 ± 1.40 and 0.79 ± 0.25, respectively, for 1960 to 2030. However, much of this slope is driven by the period after 2005, where the aerosol forcing in the CMIP projections does not consider the role of some phenomena, such as volcanic aerosols. This is of concern, as aerosols are known to strongly affect $E - P$ (Allen and Ingram 2002; Trenberth 2011; Allan et al. 2014, 2020). For the period up to 2005, the slopes are substantially weaker (0.44 ± 0.73 and 0.31 ± 0.21). Thus, the CMIP5 models suggest a nonconstant scaling slope that depends on different responses of $E - P$ and salinity to time-variable forcing, such as aerosols.

With this model uncertainty in mind, we approximately derive the $E - P$ change by multiplying the observed salinity contrast metric with the model-derived slopes for 1960–2030. The observed changes in the salinity-contrast metric (i.e., 5.2% ± 0.4% for SC2000 and 7.5% ± 0.9% for SC0) over the period 1960–2017 result in a change in the $E - P$ contrast of 7.8% ± 7.3% and 5.9% ± 2.0%, respectively. All metrics have consistent results for $E - P$ pattern amplification (the range of central estimates of $E - P$ contrast using different SC metrics is 5.2%–7.8%; see the online supplemental material for SC1000 and SC2000-q).

The slopes derived from CMIP5-Hist within 1960–2005 lead to a weaker but still positive $E - P$ contrast (2.3% ± 3.8% for SC2000, 2.3% ± 1.7% for SC0). Despite the difference in SC0, SC2000, SC1000, and SC2000-q change during 1960–2017, their derived water cycle changes are highly consistent (2.3%–2.8% for their central estimates), suggesting a robust estimate on the water cycle changes, but the uncertainty for the surface metric (SC0) is smaller because it shows a better linear correlation with $E - P$. The larger uncertainty for subsurface metrics also reveals reduced capability of models in simulating ocean subsurface properties (Cheng et al. 2016; Bilbao et al. 2019).

Furthermore, by using the observed land/ocean surface warming of 0.88 ± 0.11 K for 1960–2017 and adopting the

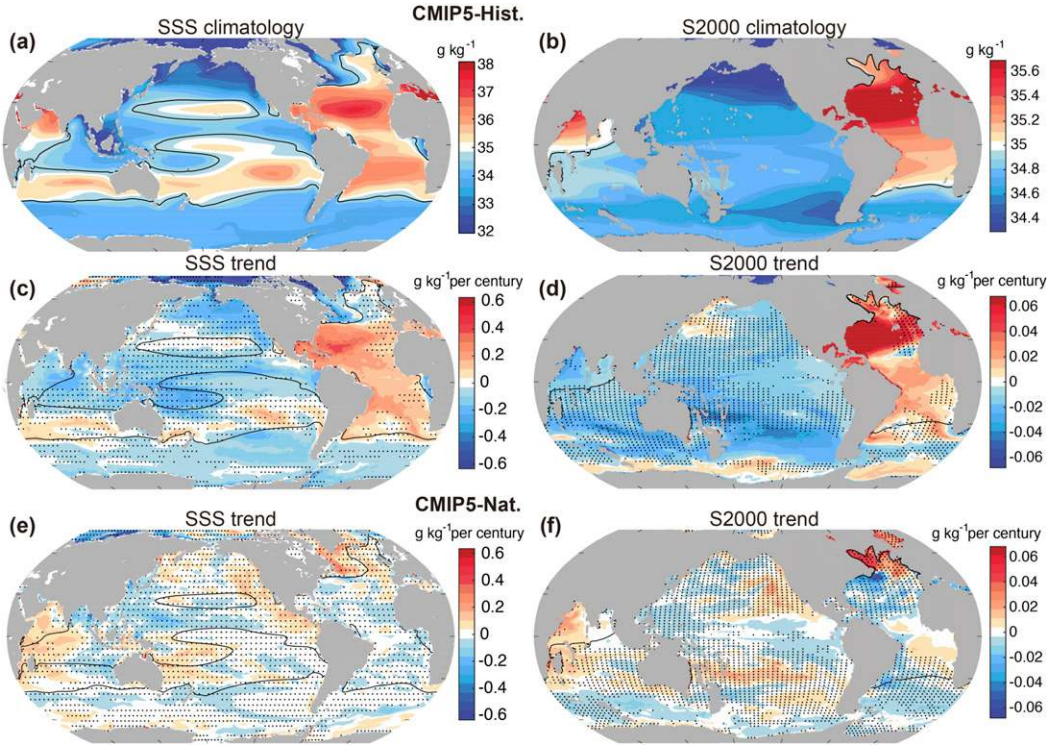

FIG. 13. Climatology and long-term ocean salinity trend from CMIP5 models, for (a)–(d) CMIP5 historical simulations and (e),(f) natural-forcing-only simulations. The linear trend is the ensemble median of the individual model results. The nonstippled regions show the signals outside the 1σ confidence level. The black contour shows the global median of the climatological salinity for SSS or S2000.

1960–2005 salinity–$E - P$ correlation, we can infer a water cycle amplification of 2.6% ± 4.4% K^{-1} using SC2000 or 2.6% ± 2.0% K^{-1} for SC0 (Table 2). Here, again, Monte Carlo simulation is used considering the additional uncertainty in GMST estimates. Our surface and subsurface salinity metrics result in very consistent central estimates of 2.6%–3.2% K^{-1} of water cycle amplification for 1960–2017 (Table 2; also see the supplemental material for SC1000 and SC2000-q).

The concept of using models to estimate $E - P$ and salinity correlations and applying this to the observed salinity change pattern to infer the associated observed water cycle amplification rate was pioneered by Durack et al. (2012), although that study explored zonal mean SSS changes and they mainly relied on CMIP future simulations to derive the salinity–$E - P$ correlations, which therefore features stronger correlations due to lack of aerosol forcing. The new SC metric-based estimates (2.6%–3.2% K^{-1}) based on improved salinity data are consistent with some of previous estimates and suggest a smaller water cycle amplification than the CC relationship (~7% K^{-1}). Skliris et al. (2016) shows water cycle amplification rates of 1.80% ± 0.78% K^{-1} for Ishii, 3.35% ± 1.44% K^{-1} for EN4, and 3.85% ± 1.64% K^{-1} for DW10 derived from the full-depth salinity change. Zika et al. (2018) combined model and full-depth EN4 data, suggesting that the water cycle has been amplified by 3.6% ± 2.1% K^{-1} from 1957 to 2016.

All of these estimates, in spite of data uncertainties, are significantly smaller than in Durack et al. (2012), suggesting a water cycle amplification of ~8% ± 5% K^{-1} warming. As the SSS pattern amplification is within 5%–8% for all studies (Table 2), besides the data difference, the discrepancy is most likely due to the derived ratio between salinity and $E - P$. In Durack et al. (2012), the SSS–($E - P$) ratio is about 1.7:1 (2:1) derived from historical simulations (historical simulations and future projections) of CMIP3 models within 1950–2000. However, the ratio of SSS and $E - P$ is about 3:1 in this study for historical simulations of CMIP5 models within 1960–2005 (corresponding to the slope of 0.31 for SC0 and $E - P$ regression). Both results featured large spread across models. Therefore, the model uncertainty and the method differences when using model results are probably responsible for the differences.

In summary, the salinity-contrast and $E - P$ contrast metrics provide a new estimate on the water cycle pattern amplification, indicating that the global water cycle has been intensified with global warming.

4. Concluding remarks

A new ocean subsurface salinity reconstruction extending from 1960 for the top 2000 m of the ocean is provided in this study. The new reconstruction overcomes key shortcomings of earlier reconstructions and has uncertainties that are much better constrained. This strongly enhances the reliability and

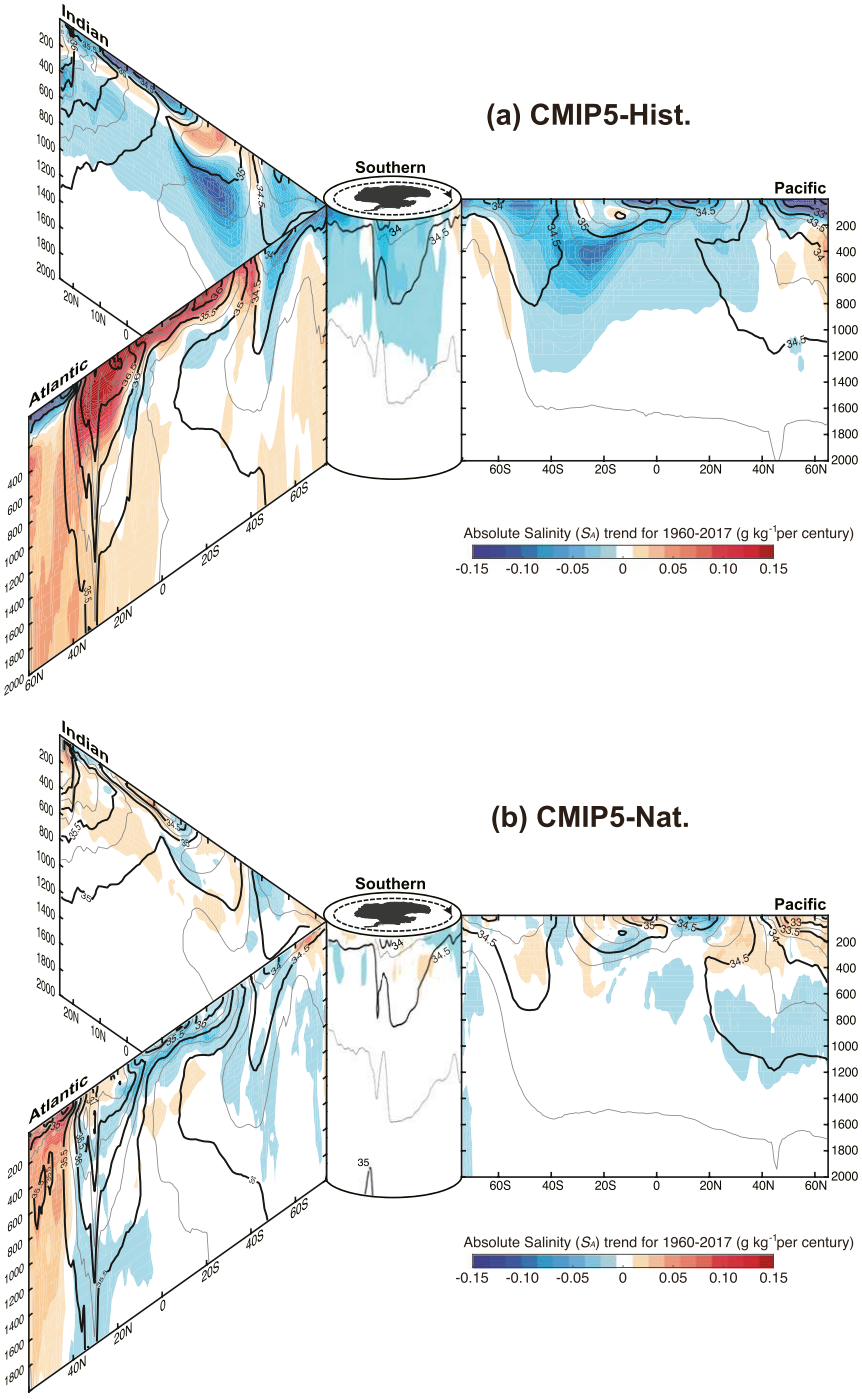

FIG. 14. Vertical section of the ocean salinity trends for 1960–2017 from sea surface to 2000 m in (a) CMIP5-Hist and (b) CMIP5-Nat simulations. Shown are the zonal mean sections in each ocean basin organized around the Southern Ocean in the center. Contours show the associated climatological mean subsurface salinity with intervals of 0.25 g kg^{-1}. (a) The ensemble median of trends for all CMIP5 historical simulations and (b) ensemble median of trends for natural-only forcing simulations are presented. RCP4.5 projections are used for the 2006–17 period, but using other scenarios does not impact the result.

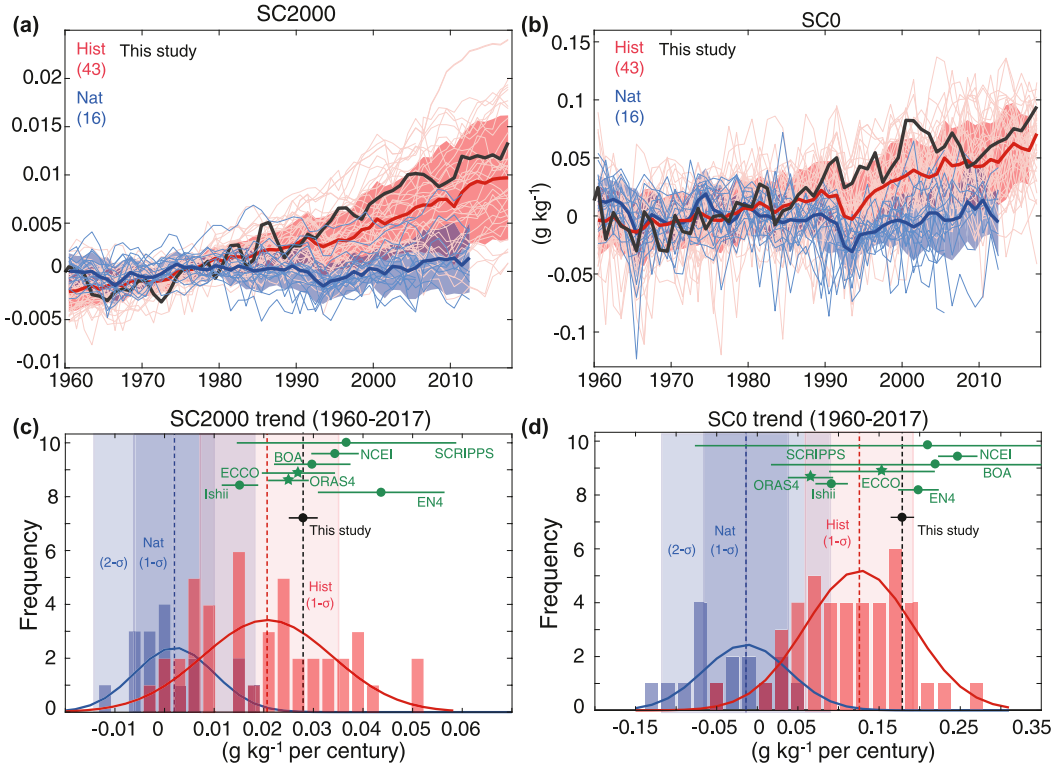

FIG. 15. Salinity changes in observations and models indexed by contrast between the high- and low-salinity regions, i.e., (left) SC2000 and (right) SC0. (a), (b), Annual mean SC2000 and SC0 time series from 1960 to 2017. The anomalies are relative to a 1960–89 baseline. (c),(d) Histograms of linear trends (1960–2017) of SC2000 and SC0 for CMIP5 Hist (and RCP4.5 within 2006–17; red) and Nat (blue) simulations. The fitted Gaussian distribution is included. The observational trend and results of seven independent datasets in green including two reanalyses (ECCO, ORAS4) and five other objective products (EN4, Ishii, BOA, NCEI, SCRIPPS) are included. All of the error ranges are 1σ spreads, but the 2σ spread for CMIP5-Nat is also shown. For the linear trend calculation, reduction in degrees of freedom is taken into account.

robustness of our key conclusions. First, we show with much more confidence than possible before, that the ocean's mean salinity pattern has been amplified, with salty regions getting saltier, and fresher regions becoming fresher. Second, we show that this trend is very likely a consequence of human activities: anthropogenic changes in the net freshwater fluxes over the past nearly 60 years have left a clear human imprint on the ocean's salinity distribution. Third, this new reconstruction also permits us to provide a more accurate constraint on the hydrological cycle changes since 1960 in combination with climate models.

Based on our analyses, we recommend using SC metrics, introduced in IPCC AR5, as regularly updated and key indicators for climate change. These metrics, especially for the subsurface (i.e., SC2000), have several distinguishing features as climate indicators: 1) their slowly evolving changes are driven by climate change and they can be used to indicate and quantify the change of global hydrological cycle; 2) their long-term changes are highly distinguishable from sampling uncertainty; and 3) it takes less than 15 (25) years for the long-term subsurface (surface) trend to emerge from background short-term fluctuations, better than (similar to) GMST changes. Cheng et al. (2018) show it takes 27 years for GMST trend to significantly emerge from background short-term fluctuations.

The remaining issues include the following:

1) The new dataset can be further improved by investigating instrumental biases in salinity observations, which needs international collaboration, because most of the old instruments were developed and used by different countries or institutions. A comparison between old bottle data from more than 100 cruises with high-quality WOCE (World Ocean Circulation Experiment) data indicates a systematic offset of $\sim 2.55 \times 10^{-3}$ psu during the period from 1970 to 1985 (Gouretski and Jancke 2000), of similar order to the observed globally averaged 0–2000 m salinity changes in this study (Fig. 5), but much smaller than the signal of the pattern amplification that we emphasize in our study. Even though we consider these potential biases as too small to affect our conclusions, more accurate salinities would permit a better quantification of the mean ocean changes. Thus, we recommend an international coordinated project for salinity data intercomparison between various instruments to identify and correct potential systematical errors.
2) The uncertainty value attached with the new salinity product mainly reveals the sampling error, and it can further be

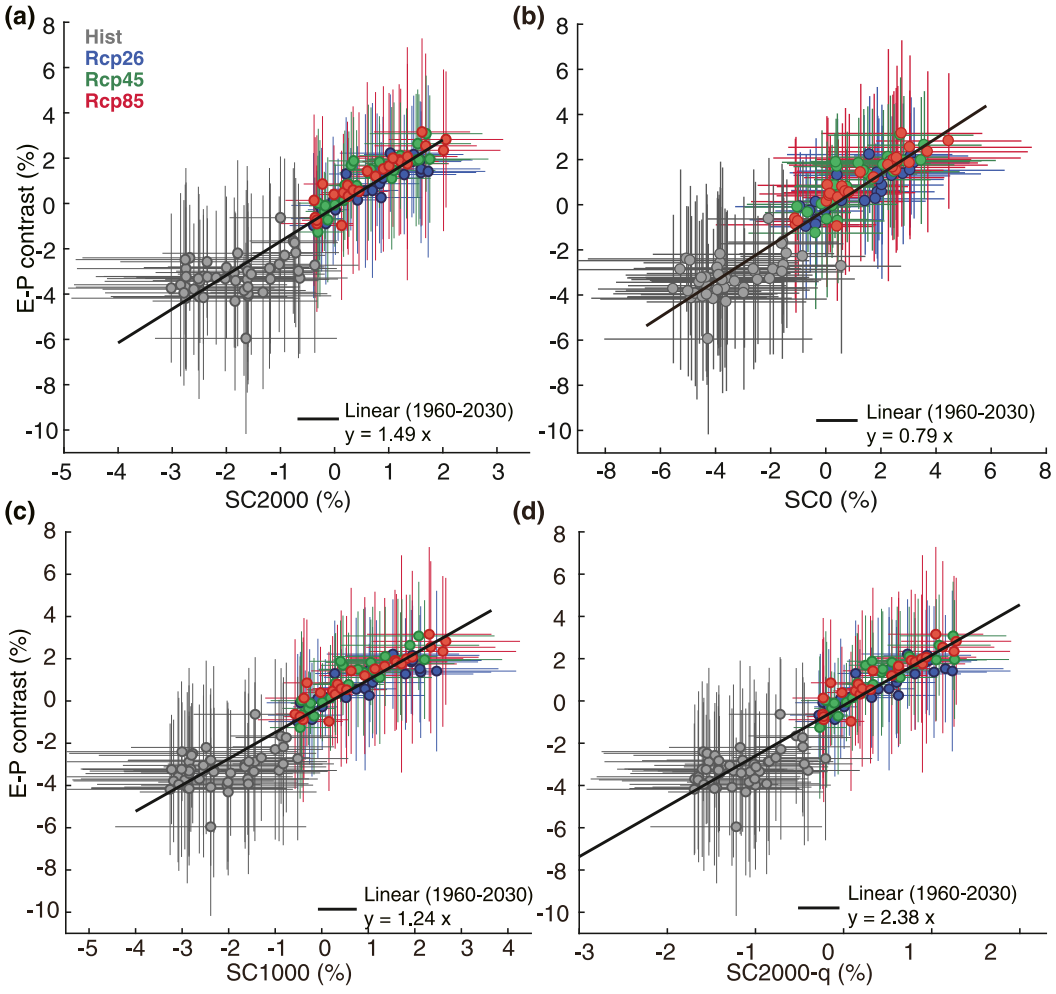

FIG. 16. Ocean salinity pattern amplification linked to $E - P$ pattern amplification. Percentage change of an index reflecting the spatial contrast in $E - P$ (y axis) vs an index reflecting the spatial contrast in ocean salinity (x axis). (a) The oceanic index computed over the top 2000 m (SC2000), as well asthe index is computed for (b) SC0, (c) SC1000, and (d) SC2000-q, respectively. All changes are percentages (%) of their climatological mean within the recent decade (2008–17). The dots are model ensemble medians, and the sticks are 1σ spread of individual models. The linear fit for CMIP5-Hist and all RCP runs within 1960–2030 is presented (black line).

improved by explicitly quantifying and adding other error sources, such as instrumental uncertainty, and errors related to data processing (i.e., use of climatology, vertical interpolation, etc.).

3) As the models show very large spread in $E - P$ and salinity simulations, quantification of hydrological cycle changes through salinity change is hampered by model uncertainty. Further refinement of the estimate can be improved by selecting better models, constraining models through observational properties, or even correcting model biases, for example, taking account of the difference in the ocean warming in different models since the strength of salinity responses partly depends on the surface warming rate and spatial patterns (Durack et al. 2012; Zika et al. 2018). Nevertheless, using models to understand the formation of the salinity change pattern will be an important follow-on works, such as Zika et al. (2018) for SSS changes.
4) Difference among various gridded products need to be better understood.
5) The uncertainty of our estimate of water cycle amplification (2.6% ± 4.4% K^{-1} using SC2000 or 2.6% ± 2.0% K^{-1} for SC0) is larger than reported in previous studies such as Skliris et al. (2016) and Zika et al. (2018). This is primarily because we took more sources of uncertainty into account and these sources are additive. Specifically, we considered three error sources: salinity data uncertainty, model uncertainty, and GMST data uncertainty, although model uncertainty dominates. Therefore, understanding model errors in simulating salinity and $E - P$

changes is critical to reduce the uncertainty in water cycle estimates.

Finally, we emphasize that the salinity changes have profound implications for the ocean system and the life it supports (Bindoff et al. 2019). For example, salinity change is one driver of ocean general circulation (Huang et al. 1992; Fedorov et al. 2004); it plays an important role in the sustainment and change of Atlantic meridional overturning circulation (Wunsch 2002). The strengthening of the salinity contrast tends to enhance ocean stratification in the high-latitude regions, amplifying the effects of ocean warming. This reduces ocean ventilation, affecting, for example, the supply of oxygen into the ocean's interior, and thus contributing substantially to ocean deoxygenation (Keeling et al. 2010). Furthermore, high-latitude freshening also tends to exacerbate ocean acidification by diluting the concentration of substances acting as buffers. Continued observations and study of salinity changes will be essential for further understanding of climate system change and its impacts (Durack et al. 2016; Vinogradova et al. 2019).

Acknowledgments. This study is supported by National Key R&D Program of China (2017YFA0603202) and Key Deployment Project of Centre for Ocean Mega-Research of Science, CAS (COMS2019Q01). N.G. acknowledges funding from the European Union's Horizon 2020 research and innovation program under grant agreements 821001 and 821003. The National Center for Atmospheric Research is sponsored by the National Science Foundation. We thank Dr. Rachel Killick, Karina von Schuckmann, and Jan Zika for helpful comments with this manuscript. Many thanks for the model data to the World Climate Research Programme's Working Group on Coupled Modelling for CMIP and the U.S. Department of Energy's Program for Climate Model Diagnosis and Intercomparison, and NOAA/NCEI and the Argo Program for ocean data. All of these data are available from the Earth System Grid Federation (ESFG; https://esgf-node.llnl.gov/projects/cmip5/). The Argo data were collected and made freely available by the International Argo Program and the national programs (http://www.argo.ucsd.edu; http://argo.jcommops.org).

Data availability statement. Salinity data produced in this study are available at http://159.226.119.60/cheng/. These data are as follows: NCEI https://www.nodc.noaa.gov/OC5/3M_HEAT_CONTENT/; Ishii (https://climate.mri-jma.go.jp/pub/ocean/ts/v7.2/); EN4 (https://www.metoffice.gov.uk/hadobs/en4/index.html); BOA and SCRIPPS (https://argo.ucsd.edu/data/argo-data-products/); ECCO (https://ecco-group.org/products-ECCO-V4r4.htm); ORAS4 (http://apdrc.soest.hawaii.edu/datadoc/ecmwf_oras4.php); DW10 (https://www.cmar.csiro.au/oceanchange/salinity.php). The authors declare no conflict of interests.

REFERENCES

Abraham, J. P., and Coauthors, 2013: A review of global ocean temperature observations: Implications for ocean heat content estimates and climate change. *Rev. Geophys.*, **51**, 450–483, https://doi.org/10.1002/rog.20022.

Adler, R. F., and Coauthors, 2018: The Global Precipitation Climatology Project (GPCP) monthly analysis (new version 2.3) and a review of 2017 global precipitation. *Atmosphere*, **9**, 138, https://doi.org/10.3390/atmos9040138.

Allan, R. P., C. Liu, M. Zahn, D. A. Lavers, E. Koukouvagias, and A. Bodas-Salcedo, 2014: Physically consistent responses of the global atmospheric hydrological cycle in models and observations. *Surv. Geophys.*, **35**, 533–552, https://doi.org/10.1007/s10712-012-9213-z.

——, and Coauthors, 2020: Advances in understanding large-scale responses of the water cycle to climate change. *Ann. N.Y. Acad. Sci.*, **1472**, 49–75, https://doi.org/10.1111/nyas.14337.

Allen, M. R., and W. J. Ingram, 2002: Constraints on future changes in climate and the hydrologic cycle. *Nature*, **419**, 228–232, https://doi.org/10.1038/nature01092.

Andrews, T., P. M. Forster, O. Boucher, N. Bellouin, and A. Jones, 2010: Precipitation, radiative forcing and global temperature change. *Geophys. Res. Lett.*, **37**, L14701, https://doi.org/10.1029/2010GL043991.

Balmaseda, M. A., K. E. Trenberth, and E. Källén, 2013: Distinctive climate signals in reanalysis of global ocean heat content. *Geophys. Res. Lett.*, **40**, 1754–1759, https://doi.org/10.1002/grl.50382.

Barnett, T. P., D. W. Pierce, and R. Schnur, 2001: Detection of anthropogenic climate change in the world's oceans. *Science*, **292**, 270–274, https://doi.org/10.1126/science.1058304.

Bilbao, R. A. F., J. M. Gregory, N. Bouttes, M. D. Palmer, and P. Stott, 2019: Attribution of ocean temperature change to anthropogenic and natural forcings using the temporal, vertical and geographical structure. *Climate Dyn.*, **53**, 5389–5413, https://doi.org/10.1007/s00382-019-04910-1.

Bindoff, N. L., and Coauthors, 2019: Changing ocean, marine ecosystems, and dependent communities. *Special Report on Ocean and Cryosphere in a Changing Climate*, H.-O. Pörtner et al., Eds., IPCC, in press.

Boyer, T. P., S. Levitus, J. I. Antonov, R. A. Locarnini, and H. E. Garcia, 2005: Linear trends in salinity for the World Ocean, 1955–1998. *Geophys. Res. Lett.*, **32**, L01604, https://doi.org/10.1029/2004GL021791.

——, and Coauthors, 2018: *World Ocean Database 2018*. A. V. Mishonov, Technical Ed., NOAA Atlas NESDIS 87, 207 pp.

Bryden, H. L., M. J. Griffiths, A. M. Lavin, R. C. Millard, G. Parrilla, and W. M. Smethie, 1996: Decadal changes in water mass characteristics at 24°N in the subtropical North Atlantic Ocean. *J. Climate*, **9**, 3162–3186, https://doi.org/10.1175/1520-0442(1996)009<3162:DCIWMC>2.0.CO;2.

Carton, J. A., G. A. Chepurin, and L. Chen, 2018: SODA3: A new ocean climate reanalysis. *J. Climate*, **31**, 6967–6983, https://doi.org/10.1175/JCLI-D-18-0149.1.

Cheng, L., and J. Zhu, 2014: Artifacts in variations of ocean heat content induced by the observation system changes. *Geophys. Res. Lett.*, **20**, 7276–7283, https://doi.org/10.1002/2014GL061881.

——, and ——, 2016: Benefits of CMIP5 multimodel ensemble in reconstructing historical ocean subsurface temperature variations. *J. Climate*, **29**, 5393–5416, https://doi.org/10.1175/JCLI-D-15-0730.1.

——, K. E. Trenberth, M. D. Palmer, J. Zhu, and J. P. Abraham, 2016: Observed and simulated full-depth ocean heat-content changes for 1970–2005. *Ocean Sci.*, **12**, 925–935, https://doi.org/10.5194/os-12-925-2016.

——, ——, J. Fasullo, T. Boyer, J. Abraham, and J. Zhu, 2017: Improved estimates of ocean heat content from 1960 to 2015. *Sci. Adv.*, **3**, e1601545, https://doi.org/10.1126/sciadv.1601545.

——, ——, ——, J. Abraham, T. P. Boyer, K. von Schuckmann, and J. Zhu, 2018: Taking the pulse of the planet. *Eos, Trans.*

Amer. Geophys. Union, **98**, 14–16, https://doi.org/10.1029/2017EO081839.

——, J. Abraham, Z. Hausfather, and K. E. Trenberth, 2019: How fast are the oceans warming? *Science*, **363**, 128–129, https://doi.org/10.1126/science.aav7619.

Cowtan, K., and R. Way, 2013: Coverage bias in the HadCRUT4 temperature series and its impact on recent temperature trends. *Quart. J. Roy. Meteor. Soc.*, **140**, 1935–1944, https://doi.org/10.1002/QJ.2297.

Cravatte, S., T. Delcroix, D. Zhang, M. McPhaden, and J. Leloup, 2009: Observed freshening and warming of the western Pacific warm pool. *Climate Dyn.*, **33**, 565–589, https://doi.org/10.1007/s00382-009-0526-7.

Curry, R., B. Dickson, and I. Yashayaev, 2003: A change in the freshwater balance of the Atlantic Ocean over the past four decades. *Nature*, **426**, 826–829, https://doi.org/10.1038/nature02206.

Dangendorf, S., M. Marcos, G. Wöppelmann, C. P. Conrad, T. Frederikse, and R. Riva, 2017: Reassessment of 20th century global mean sea level rise. *Proc. Natl. Acad. Sci. USA*, **114**, 5946–5951, https://doi.org/10.1073/pnas.1616007114.

DeAngelis, A. M., X. Qu, M. D. Zelinka, and A. Hall, 2015: An observational radiative constraint on hydrologic cycle intensification. *Nature*, **528**, 249–253, https://doi.org/10.1038/nature15770.

Delcroix, T., S. Cravatte, and M. J. McPhaden, 2007: Decadal variations and trends in tropical Pacific sea surface salinity since 1970. *J. Geophys. Res.*, **112**, C03012, https://doi.org/10.1029/2006JC003801.

Du, Y., and Coauthors, 2015: Decadal trends of the upper ocean salinity in the tropical Indo-Pacific since mid-1990s. *Sci. Rep.*, **5**, 16050, https://doi.org/10.1038/srep16050.

Durack, P. J., 2015: Ocean salinity and the global water cycle. *Oceanography*, **28**, 20–31, https://doi.org/10.5670/oceanog.2015.03.

——, and S. E. Wijffels, 2010: Fifty-year trends in global ocean salinities and their relationship to broad-scale warming. *J. Climate*, **23**, 4342–4362, https://doi.org/10.1175/2010JCLI3377.1.

——, ——, and R. J. Matear, 2012: Ocean salinities reveal strong global water cycle intensification during 1950 to 2000. *Science*, **336**, 455–458, https://doi.org/10.1126/science.1212222.

——, P. J. Gleckler, F. Landerer, and K. E. Taylor, 2014: Quantifying underestimates of long-term upper-ocean warming. *Nat. Climate Change*, **4**, 999–1005, https://doi.org/10.1038/nclimate2389.

——, T. Lee, N. T. Vinogradova, and D. Stammer, 2016: Keeping the lights on for global ocean salinity observation. *Nat. Climate Change*, **6**, 228–231, https://doi.org/10.1038/nclimate2946.

Fedorov, A. V., R. C. Pacanowski, S. G. Philander, and G. Boccaletti, 2004: The effect of salinity on the wind-driven circulation and the thermal structure of the upper ocean. *J. Phys. Oceanogr.*, **34**, 1949–1966, https://doi.org/10.1175/1520-0485(2004)034<1949:TEOSOT>2.0.CO;2.

Forget, G., J.-M. Campin, P. Heimbach, C. Hill, R. Ponte, and C. Wunsch, 2015: ECCO version 4: An integrated framework for non-linear inverse modeling and global ocean state estimation. *Geosci. Model Dev.*, **8**, 3071–3104, https://doi.org/10.5194/gmd-8-3071-2015.

Foster, G., and S. Rahmstorf, 2011: Global temperature evolution 1979–2010. *Environ. Res. Lett.*, **6**, 044022, https://doi.org/10.1088/1748-9326/6/4/044022.

GISTEMP, 2019: Surface Temperature Analysis, NASA Goddard Institute for Space Studies, accessed 30 November 2019, https://data.giss.nasa.gov/gistemp/.

Good, S. A., M. J. Martin, and N. A. Rayner, 2013: EN4: Quality controlled ocean temperature and salinity profiles and monthly objective analyses with uncertainty estimates. *J. Geophys. Res. Oceans*, **118**, 6704–6716, https://doi.org/10.1002/2013JC009067.

Gouretski, V. V., and K. Jancke, 2000: Systematic errors as the cause for an apparent deep water property variability: Global analysis of the WOCE and historical hydrographic data. *Prog. Oceanogr.*, **48**, 337–402, https://doi.org/10.1016/S0079-6611(00)00049-5.

Gruber, N., and Coauthors, 2019: The oceanic sink for anthropogenic CO_2 from 1994 to 2007. *Science*, **363**, 1193–1199, https://doi.org/10.1126/science.aau5153.

Haumann, F. A., N. Gruber, M. Münnich, I. Frenger, and S. Kern, 2016: Sea-ice transport driving Southern Ocean salinity and its recent trends. *Nature*, **537**, 89–92, https://doi.org/10.1038/nature19101.

Hegerl, G. C., and Coauthors, 2015: Challenges in quantifying changes in the global water cycle. *Bull. Amer. Meteor. Soc.*, **96**, 1097–1115, https://doi.org/10.1175/BAMS-D-13-00212.1.

Held, I. M., and B. J. Soden, 2006: Robust responses of the hydrological cycle to global warming. *J. Climate*, **19**, 5686–5699, https://doi.org/10.1175/JCLI3990.1.

Helm, K. P., N. L. Bindoff, and J. A. Church, 2010: Changes in the global hydrological-cycle inferred from ocean salinity. *Geophys. Res. Lett.*, **37**, L18701, https://doi.org/10.1029/2010GL044222.

Hosoda, S., T. Suga, N. Shikama, and K. Mizuno, 2009: Global surface layer salinity change detected by Argo and its implication for hydrological cycle intensification. *J. Oceanogr.*, **65**, 579–586, https://doi.org/10.1007/s10872-009-0049-1.

Huang, R. X., J. R. Luyten, and H. M. Stommel, 1992: Multiple equilibrium states in combined thermal and saline circulation. *J. Phys. Oceanogr.*, **22**, 231–246, https://doi.org/10.1175/1520-0485(1992)022<0231:MESICT>2.0.CO;2.

IPCC, 2019: Summary for policymakers. *IPCC Special Report on the Ocean and Cryosphere in a Changing Climate*, H.-O. Pörtner et al., Eds., in press.

IQuOD Team, 2018: International Quality Controlled Ocean Database (IQuOD) version 0.1—Aggregated and community quality controlled ocean profile data 1772-2018 (NCEI Accession 0170893). NOAA National Centers for Environmental Information, accessed August 2019, https://doi.org/10.7289/V51R6NSF.

Ishii, M., M. Kimoto, and M. Kachi, 2003: Historical ocean subsurface temperature analysis with error estimates. *Mon. Wea. Rev.*, **131**, 51–73, https://doi.org/10.1175/1520-0493(2003)131<0051:HOSTAW>2.0.CO;2.

——, A. Shouji, S. Sugimoto, and T. Matsumoto, 2005: Objective analyses of sea-surface temperature and marine meteorological variables for the 20th century using ICOADS and the Kobe Collection. *Int. J. Climatol.*, **25**, 865–879, https://doi.org/10.1002/joc.1169.

——, Y. Fukuda, S. Hirahara, S. Yasui, T. Suzuki, and K. Sato, 2017: Accuracy of global upper ocean heat content estimation expected from present observational data sets. *SOLA*, **13**, 163–167, https://doi.org/10.2151/SOLA.2017-030.

Keeling, R. F., A. Körtzinger, and N. Gruber, 2010: Ocean deoxygenation in a warming world. *Annu. Rev. Mar. Sci.*, **2**, 199–229, https://doi.org/10.1146/annurev.marine.010908.163855.

Levitus, S., and Coauthors, 2012: World ocean heat content and thermosteric sea level change (0–2000 m), 1955–2010. *Geophys. Res. Lett.*, **39**, L10603, https://doi.org/10.1029/2012GL051106.

Li, H., F. Xu, W. Zhou, D. Wang, J. S. Wright, Z. Liu, and Y. Lin, 2017: Development of a global gridded Argo data set with Barnes successive corrections. *J. Geophys. Res. Oceans*, **122**, 866–889, https://doi.org/10.1002/2016JC012285.

Marvel, K., M. Biasutti, C. Bonfils, K. E. Taylor, Y. Kushnir, and B. I. Cook, 2017: Observed and projected changes to the precipitation annual cycle. *J. Climate*, **30**, 4983–4995, https://doi.org/10.1175/JCLI-D-16-0572.1.

McDougall, T. J., D. R. Jackett, F. J. Millero, R. Pawlowicz, and P. M. Barker, 2012: A global algorithm for estimating Absolute Salinity. *Ocean Sci.*, **8**, 1123–1134, https://doi.org/10.5194/os-8-1123-2012.

Meyssignac, B., and Coauthors, 2019: Measuring global ocean heat content to estimate the Earth energy imbalance. *Front. Mar. Sci.*, **6**, 432, https://doi.org/10.3389/FMARS.2019.00432.

Palmer, M. D., and Coauthors, 2015: Ocean heat content variability and change in an ensemble of ocean reanalyses. *Climate Dyn.*, **49**, 909–930, https://doi.org/10.1007/s00382-015-2801-0.

Palmer, T., and B. Stevens, 2019: The scientific challenge of understanding and estimating climate change. *Proc. Natl. Acad. Sci. USA*, **116**, 24 390–24 395, https://doi.org/10.1073/pnas.1906691116.

Pierce, D. W., P. J. Gleckler, T. P. Barnett, B. D. Santer, and P. J. Durack, 2012: The fingerprint of human-induced changes in the ocean's salinity and temperature fields. *Geophys. Res. Lett.*, **39**, L21704, https://doi.org/10.1029/2012GL053389.

Reagan, J., D. Seidov, and T. Boyer, 2018: Water vapor transfer and near-surface salinity contrasts in the North Atlantic Ocean. *Sci. Rep.*, **8**, 8830, https://doi.org/10.1038/s41598-018-27052-6.

Reverdin, G., and Coauthors, 2019: North Atlantic extratropical and subpolar gyre variability during the last 120 years: A gridded dataset of surface temperature, salinity, and density. Part I: Dataset validation and RMS variability. *Ocean Dyn.*, **69**, 385–403, https://doi.org/10.1007/s10236-018-1240-y.

Rhein, M., and Coauthors, 2013: Observations: Ocean. *Climate Change 2013: The Physical Science Basis*, T. F. Stocker et al., Eds., Cambridge University Press,, 255–315.

Riser, S. C., and Coauthors, 2016: Fifteen years of ocean observations with the global Argo array. *Nat. Climate Change*, **6**, 145–153, https://doi.org/10.1038/nclimate2872.

Roemmich, D., and J. Gilson, 2009: The 2004–2008 mean and annual cycle of temperature, salinity, and steric height in the global ocean from the Argo Program. *Prog. Oceanogr.*, **82**, 81–100, https://doi.org/10.1016/j.pocean.2009.03.004.

Rohde, R., R. Muller, R. Jacobsen, S. Perlmutter, and S. Mosher, 2013: Berkeley Earth temperature averaging process. *Geoinfor. Geostat. Overview*., 1 (2), https://doi.org/10.4172/gigs.1000103.

Sakov, P., and P. R. Oke, 2008a: Implications of the form of the ensemble transformation in the ensemble square root filters. *Mon. Wea. Rev.*, **136**, 1042–1053, https://doi.org/10.1175/2007MWR2021.1.

——, and ——, 2008b: A deterministic formulation of the ensemble Kalman filter: An alternative to ensemble square root filters. *Tellus*, **60A**, 361–371, https://doi.org/10.1111/j.1600-0870.2007.00299.x.

Schmitt, R. W., 2008: Salinity and the global water cycle. *Oceanography*, **21**, 12–19, https://doi.org/10.5670/oceanog.2008.63.

Sen Gupta, A., N. Jourdain, J. Brown, and D. Monselesan, 2013: Climate drift in the CMIP5 models. *J. Climate*, **26**, 8597–8615, https://doi.org/10.1175/JCLI-D-12-00521.1.

Skliris, N., R. Marsh, S. A. Josey, S. A. Good, C. Liu, and R. P. Allan, 2014: Salinity changes in the world ocean since 1950 in relation to changing surface freshwater fluxes. *Climate Dyn.*, **43**, 709–736, https://doi.org/10.1007/s00382-014-2131-7.

——, J. D. Zika, G. Nurser, S. A. Josey, and R. Marsh, 2016: Global water cycle amplifying at less than the Clausius-Clapeyron rate. *Sci. Rep.*, **6**, 38752, https://doi.org/10.1038/srep38752.

——, R. Marsh, J. Mecking, and J. Zika, 2020: Changing water cycle and freshwater transports in the Atlantic Ocean in observations and CMIP5 models. *Climate Dyn.*, **54**, 4971–4989, https://doi.org/10.1007/s00382-020-05261-y.

Stott, P. A., R. T. Sutton, and D. M. Smith, 2008: Detection and attribution of Atlantic salinity changes. *Geophys. Res. Lett.*, **35**, L21702, https://doi.org/10.1029/2008GL035874.

Sun, F., M. L. Roderick, and G. D. Farquhar, 2012: Changes in the variability of global land precipitation. *Geophys. Res. Lett.*, **39**, L19402, https://doi.org/10.1029/2012GL053369.

Sverdrup, H. U., M. W. Johnson, and R. W. Fleming, 1942: *The Oceans: Their Physics, Chemistry and General Biology*. Prentice-Hall, 1087 pp.

Swart, N. C., S. T. Gille, J. C. Fyfe, and N. P. Gillett, 2018: Recent Southern Ocean warming and freshening driven by greenhouse gas emissions and ozone depletion. *Nat. Geosci.*, **11**, 836–841, https://doi.org/10.1038/s41561-018-0226-1.

Sy, A., and H.-H. Hinrichsen, 1986: The influence of long-term storage on the salinity of bottled seawater samples. *Dtsch. Hydrogr. Z.*, **39**, 35–40, https://doi.org/10.1007/BF02330522.

Tapley, B. D., and Coauthors, 2019: Contributions of GRACE to understanding climate change. *Nat. Climate Change*, **9**, 358–369, https://doi.org/10.1038/s41558-019-0456-2.

Taylor, K. E., R. J. Stouffer, and G. A. Meehl, 2012: An overview of CMIP5 and the experiment design. *Bull. Amer. Meteor. Soc.*, **93**, 485–498, https://doi.org/10.1175/BAMS-D-11-00094.1.

Terray, L., L. Corre, S. Cravatte, T. Delcroix, G. Reverdin, and A. Ribes, 2012: Near-surface salinity as nature's rain gauge to detect human influence on the tropical water cycle. *J. Climate*, **25**, 958–977, https://doi.org/10.1175/JCLI-D-10-05025.1.

Trenberth, K. E., 2011: Changes in precipitation with climate change. *Climate Res.*, **47**, 123–138, https://doi.org/10.3354/cr00953.

——, and J. Fasullo, 2013: Regional energy and water cycles: Transports from ocean to land. *J. Climate*, **26**, 7837–7851, https://doi.org/10.1175/JCLI-D-13-00008.1.

——, A. Dai, R. M. Rasmussen, and D. B. Parsons, 2003: The changing character of precipitation. *Bull. Amer. Meteor. Soc.*, **84**, 1205–1218, https://doi.org/10.1175/BAMS-84-9-1205.

——, L. Smith, T. Qian, A. Dai, and J. Fasullo, 2007: Estimates of the global water budget and its annual cycle using observational and model data. *J. Hydrometeor.*, **8**, 758–769, https://doi.org/10.1175/JHM600.1.

——, J. Fasullo, K. von Schuckmann, and L. Cheng, 2016: Insights into Earth's energy imbalance from multiple sources. *J. Climate*, **29**, 7495–7505, https://doi.org/10.1175/JCLI-D-16-0339.1.

Vinogradova, N. T., and R. M. Ponte, 2017: In search of fingerprints of the recent intensification of the ocean water cycle. *J. Climate*, **30**, 5513–5528, https://doi.org/10.1175/JCLI-D-16-0626.1.

——, and Coauthors, 2019: Satellite salinity observing system: Recent discoveries and the way forward. *Front. Mar. Sci.*, **6**, 243, https://doi.org/10.3389/fmars.2019.00243.

Vose, R. S., R. Adler, G. Gu, A. Becker, X. Yin, and M. Bosilovich, 2019: Precipitation [in "State of the Climate in 2018"]. *Bull. Amer. Meteor. Soc.*, **100** (9), S29–S30, https://doi.org/10.1175/2019BAMSSTATEOFTHECLIMATE.1.

Wang, G., L. Cheng, J. Abraham, and C. Li, 2017a: Consensuses and discrepancies of basin-scale ocean heat content changes in different ocean analyses. *Climate Dyn.*, **50**, 2471–2487, https://doi.org/10.1007/s00382-017-3751-5.

——, ——, T. Boyer, and C. Li, 2017b: Halosteric sea level changes during the Argo era. *Water*, **9**, 484, https://doi.org/10.3390/w9070484.

Watanabe, M., Y. Kamae, H. Shiogama, A. M. DeAngelis, and K. Suzuki, 2018: Low clouds link equilibrium climate sensitivity to hydrological sensitivity. *Nat. Climate Change*, **8**, 901–906, https://doi.org/10.1038/s41558-018-0272-0.

Wunsch, C., 2002: What is the thermohaline circulation? *Science*, **298**, 1179–1181, https://doi.org/10.1126/science.1079329.

Wust, G., 1936: Oberflachensalzgehalt, Verdunstung und Niederschlag auf den Weltmeere, Landerkundliche Forschung. *Festschrift für Norbert Krebs*, 347–359.

Yu, L., 2011: A global relationship between the ocean water cycle and near-surface salinity. *J. Geophys. Res.*, **116**, C10025, https://doi.org/10.1029/2010JC006937.

——, S. Josey, F. Bingham, and T. Lee, 2020: Intensification of the global water cycle and evidence from ocean salinity: A synthesis review. *Ann. N. Y. Acad. Sci.*, **1472**, 76–94, https://doi.org/10.1111/nyas.14354.

Zang, X., and C. Wunsch, 2001: Spectral description of low-frequency oceanic variability. *J. Phys. Oceanogr.*, **31**, 3073–3095, https://doi.org/10.1175/1520-0485(2001)031<3073:SDOLFO>2.0.CO;2.

Zika, J. D., N. Skliris, A. J. G. Nurser, S. A. Josey, L. Mudryk, F. Laliberté, and R. Marsh, 2015: Maintenance and broadening of the ocean's salinity distribution by the water cycle. *J. Climate*, **28**, 9550–9560, https://doi.org/10.1175/JCLI-D-15-0273.1.

——, ——, T. A. Blaker, R. Marsh, A. J. G. Nurser, and S. A. Josey, 2018: Improved estimates of water cycle change from ocean salinity: The key role of ocean warming. *Environ. Res. Lett.*, **13**, 074036, https://doi.org/10.1088/1748-9326/aace42.